MICROMECHANICAL CHARACTERIZATION OF METALLIC GLASS — CRYSTALLINE NANOCOMPOSITE COATINGS

A THESIS SUBMITTED TO
THE GRADUATE SCHOOL OF NATURAL AND APPLIED SCIENCES
OF
MIDDLE EAST TECHNICAL UNIVERSITY

BY

MOHAMMAD ABBOUD

IN PARTIAL FULFILLMENT OF THE REQUIREMENTS
FOR
THE DEGREE OF MASTER OF SCIENCE
IN
MICRO AND NANOTECHNOLOGY

DECEMBER 2018

Approval of the thesis:

MICROMECHANICAL CHARACTERIZATION OF METALLIC GLASS — CRYSTALLINE NANOCOMPOSITE COATINGS

submitted by **MOHAMMAD ABBOUD** in partial fulfillment of the requirements for the degree of **Master of Science in Micro and Nanotechnology, Middle East Technical University** by,

Prof. Dr. Halil Kalıpçılar
Dean, Graduate School of **Natural and Applied Sciences** _____

Assoc. Prof. Almıla Güvenç Yazıcıoğlu
Head of Department, **Micro and Nanotechnology, METU** _____

Asst. Prof. Dr. Sezer Özerinç
Supervisor, **Mechanical Engineering Dept.**, **METU** _____

Assoc. Prof. Dr. Y. Eren Kalay
Co-Supervisor, **Met. and Mat. Eng. Dept., METU** _____

Examining Committee Members:

Prof. Dr. İshak Karakaya
Metallurgical and Materials Eng. Dept., METU _____

Asst. Prof. Dr. Sezer Özerinç
Mechanical Eng. Dept., METU _____

Assoc. Prof. Dr. Y. Eren Kalay
Metallurgical and Materials Eng. Dept., METU _____

Asst. Prof. Dr. Batur Ercan
Metallurgical and Materials Eng. Dept., METU _____

Asst. Prof. Dr. Caner Şimşir
Manufacturing Eng. Dept., Atilim University _____

Date: 21.12.2018

I hereby declare that all information in this document has been obtained and presented in accordance with academic rules and ethical conduct. I also declare that, as required by these rules and conduct, I have fully cited and referenced all material and results that are not original to this work.

Name, Last name: Mohammad ABBOUD

Signature:

ABSTRACT

MICROMECHANICAL CHARACTERIZATION OF METALLIC GLASS — CRYSTALLINE NANOCOMPOSITE COATINGS

Abboud, Mohammad
M.Sc., Micro and Nanotechnology
Supervisor: Asst. Prof. Dr. Sezer Özerinç
Co-Supervisor: Assoc. Prof. Dr. Y. Eren Kalay

December 2018, 93 pages

Amorphous/crystalline nanolayers provide an effective model system to study the mechanical behavior and size effects of metallic glasses and crystalline metals in confined geometries. They also provide an advantageous structure for improving the ductility of amorphous metals while maintaining their outstanding strength. Combination of high strength and ductility make these nanocomposites promising materials as wear resistant coatings.

The structure-property relationship in Amorphous/Crystalline nanolayers containing HCP crystalline layers were investigated. CuTi/Ti and CuZr/Zr nanolayers were prepared by magnetron sputtering with layer thicknesses in the range 10–100 nm. The mechanical properties of these nanolayers were investigated using nanoindentation technique, while the wear resistance of CuZr/Zr was investigated using nanoscratch technique. X-Ray diffraction (XRD), Scanning Electron Microscopy (SEM), Energy Dispersive Spectroscopy (EDS), Transmission Electron Microscopy (TEM), and High-Resolution Transmission Electron Microscopy (HRTEM) were used to characterize the structure and composition of the films.

The hardness of the CuTi/Ti and CuZr/Zr nanolayers were close to those of the monolithic CuTi and CuZr, respectively. The hardness remained virtually the same for different layer thicknesses as opposed to CuTi/Cu amorphous/FCC crystalline nanolayers which exhibit increasing strength with decreasing layer thickness. The results can be explained by the confined layer slip model that predicts an effective flow stress for HCP crystalline layers higher than those of the amorphous layers. As a result, the strength and size-effects are governed by the mechanical behavior of the softer amorphous layer.

The scratch resistance was the highest for the monolithic CuZr, and diminished with decreasing layer thickness for nanolayered coatings, although hardness and elastic modulus were independent of layer thickness. The nanocomposite with layer thickness of 10 nm did not show any sign of failure in spite of compressive strain exceeding 80%. Low shear strength of the CuZr-Zr interface and strain hardening of Zr layers can explain the layer thickness dependent wear resistance and outstanding damage tolerance observed. Layered metallic glass/crystalline nanocomposites combine high hardness and resistance to fracture, providing a new design space for the development of effective wear resistant coatings.

Keywords: metallic glasses, thin films, nanolayered metals, wear resistant coatings, nanoscratch testing, nanoindentation

ÖZ

METALİK CAM — KRİSTAL NANOKOMPOZİT KAPLAMALARIN MİKROMEKANİK KARAKTERİZASYONU

Abboud, Mohammad
Yüksek Lisans, Mikro ve Nanoteknoloji
Tez Yöneticisi: Doktor Öğretim Üyesi Sezer Özerinç
Ortak Tez Yöneticisi: Doçent Doktor Yunus Eren Kalay

Aralık 2018, 93 sayfa

Amorf/kristal nanokatmanlar sınırlandırılmış geometrideki metalik camların ve kristal metallerin mekanik davranışının ve boyut etkilerinin çalışılması için etkin bir model sistemi sağlar. Ayrıca bu tarz nanokatmanlar yüksek mukavemeti sürdürürken amorf metallerin sünekliğini geliştirmek için avantajlı bir yapı sağlar. Yüksek mukavemetin ve sünekliğin birleştirilmesi bu nanokompozitleri aşınmaya karşı dirençli kaplamalar olarak gelecek vadeden malzeme yapar.

HCP kristal katmanları içeren amorf/kristal nanokatmanların yapı-özellik ilişkileri incelendi. Katman kalınlığı 10–100 nm aralığında değişen CuTi/Ti ve CuZr/Zr nano-katmanlar magnetron püskürtme ile hazırlandı. Nanosertlik tekniğiyle bu katmanların mekanik özellikleri ve nanoçizik testiyle CuZr/Zr nanokatmanların aşınmaya karşı direnci incelendi. Filmlerin yapısı ve kompozisyonu X-ışını kırınımı, Taramalı Elektron Mikroskopi, Enerji Dispersif Spektroskopi, Geçirimli Elektron Mikroskopi ve Yüksek Çözünürlüklü Geçirimli Elektron Mikroskopi teknikleri kullanılarak karakterize edildi.

CuTi/Ti ve CuZr/Zr nanokatmanlarının sertliği sırasıyla monolitik CuTi ve CuZr'unkine yakındı. Katman kalınlığı azalırken artan mukavemet gösteren literatürdeki CuTi/Cu amorf/FCC kristal nanokatmanlara karşın yaptığımız amorf/HCP kristalin farklı katman kalınlıkları için sertliği nerdeyse sabit kaldı. Sonuçlar, HCP kristal katmanlarının amorf katmanlara kıyasla daha yüksek etkili akma gerilimini öngören sınırlandırılmış katman kayma modeliyle açıklanabilir. Sonuç olarak, mukavemet ve boyut etkileri daha yumuşak amorf katmanların mekanik davranışıyla kontrol edilir.

Monolitik CuZr en yüksek çizme direncine sahiptir, ama nanokatmanlı kaplamalar sertliğin ve elastik modülüsün katman kalınlığına bağlı olmamasına rağmen katman kalınlığı azalırken çizme direnci azalır. Kompresif gerginliği %80'i aşmasına rağmen, 10 nm katman kalınlığına sahip olan nanokompozit herhangi bir delaminasyon belirtisi göstermedi. CuZr/Zr'un ara yüzeyinin düşük kesme gerilimi ve Zr katmanlarının gerinim sertleşmesi, katman kalınlığına bağlı aşınma direncini ve yüksek hasar toleransını açıklayabilir. Katmanlı metalik cam / kristal nanokompozitler, yüksek sertlik ve kırılmaya karşı direncin birleştirilmesinde, etkili aşınmaya dirençli kaplamaların geliştirilmesi için yeni bir tasarım alanı sağlar.

Anahtar Kelimeler: metalik camlar, ince filmler, nanokatmanlı metaller, nano-çizik testi, nanosertlik

Dedicated to My Family and My Girlfriend

ACKNOWLEDGEMENTS

Firstly, I would like to express my gratitude to my supervisor, Assist. Prof. Dr. Sezer Özerinç for his patient guidance, enthusiastic encouragement and useful critiques of this research work. It has been an honor to be his student.

Secondly, I would like to thank my co-advisor Assoc. Prof. Dr. Eren Kalay for his guidance and experience-sharing especially in the XRD characterization and electron microscopy.

I am grateful to Servet Şehirli for sharing his experiences, thoughts, and dedication. I would like to thank Alican Alpkaya, Alim Yolalmaz, Burçin Kaygusuz, Mehmet Kepenekçi, and Sencer Aydın firstly for their friendship and secondly for their helpful discussions on the experiments and data analyses.

I would like to thank Dr. Amir Motallebzadeh for helping me do some of the experiments. I am also grateful to METU Central Laboratory and Bilkent UNAM staff for their technical help.

Finally, I would like to thank my family and my girlfriend. I am grateful to them for providing me the confidence needed for becoming successful and for motivating me on the challenging paths every time I struggled.

The author acknowledges the financial support provided from TÜBİTAK 3501 CAREER Award under Project No. 116M429, ODTÜ BAP under Project No GAP-302-2018-2662 and ODTÜ BAP under Project No BAP-08-11-2016-072.

TABLE OF CONTENTS

LIST OF TABLES

LIST OF FIGURES

LIST OF SYMBOLS

H	hardness
P	load
P_{max}	peak indentation load
S	stiffness of the initial part of the unloading
h_f	final depth after unloading
h_{max}	maximum hardness
h_c	contact depth
A_p	projected area
ϵ	Sneddon's equation constant
θ	angle of incidence
n	diffraction order
hkl	crystalline plane
d	interatomic distance
λ	wavelength of the incident x-ray beam
K	dimensionless value representing the shape factor
B	full width of the associated diffraction peak at half maximum
L	crystallite size
E	elastic modulus
M	Taylor factor
μ	effective shear modulus
b	length of the Burgers vector
v	Poisson's ratio
h	layer thickness
φ	angle between the glide plane and the interface
α	core cutoff parameter
f	interface stress

ABBREVIATIONS

A	amorphous
AFM	atomic force microscopy
ASTM	American Society for Testing and Materials
BCC	body centered cubic
C	crystalline
CLS	confined layer slip
CRSS	critical resolved shear stress
DC	Direct Current
EDS	energy-dispersive x-ray spectroscopy
exp	experimental data
FCC	face centered cubic
FIB	focused ion beam
FWHM	full width half maximum
HCP	hexagonally close packed
MG	metallic glasses
PVD	physical vapor deposition
RF	Radio Frequency
SEM	scanning electron microscopy
SS	316L Stainless Steel
STZ	shear transformation zones
TEM	transmission electron microscopy
WDS	wavelength-dispersive x-ray spectroscopy
XRD	X-ray diffraction

CHAPTER 1

1. INTRODUCTION

Metallic glasses (MGs) are amorphous alloys that exhibit a wide range of desirable properties such as outstanding strength, high elastic limit, and corrosion resistance [1]. They have been widely studied for the last four decades, as these unique properties make them promising materials for engineering applications [1–3]. Thin film metallic glasses constitute a special category of MGs that are obtained by the deposition of an MG alloy on a substrate and have recently attracted attention both from a scientific and practical perspective [4]. Very high cooling rates provided by deposition techniques such as magnetron sputtering enables the preparation of fully amorphous structures for a wide range of alloys and compositions that are difficult or impossible to synthesize through solidification techniques. While thin film MGs facilitates fundamental studies of structure-property relationships in MGs, the unique properties of thin film MGs also offer opportunities from an application point of view. Defect-free and isotropic nature of MGs combined with high elastic limits and formability at the nanoscale make them promising materials for MEMS industry [5]. In addition, the wide design space offered by MGs combined with the lack of grain boundaries provide an opportunity for the development of wear resistant, corrosion resistant and biocompatible coatings.

One of the major drawbacks that have so far limited the practical use of MGs is their brittle nature. In bulk MGs, shear transformation zones (STZs) mediate plasticity [6]. The percolation of these zones results in shear bands – deformation zones with shear softening behavior, causing catastrophic failure [7]. One of the approaches to overcoming this problem is to introduce a crystalline or amorphous second phase in the MG matrix, which hinders the catastrophic propagation of a single shear band [8].

For thin film MGs, an analogous approach for ductility improvements has been the utilization of alternating layers of amorphous and crystalline structures in the form of nanolayered composites [9,10]. Previous work has shown that these nanolayered composites can improve the ductility by hindering the propagation of shear bands and promoting co-deformation of the amorphous and the crystalline layers [11]. Replacing the monolithic MG with a nanolayered amorphous-crystalline composite usually results in a compromise between the higher strength of the MG and the higher ductility of the crystalline layers [12].

This thesis focuses on understanding the mechanical properties of nanolaminates and aims at improving their hardness and scratch resistance by either changing the individual layer thicknesses or the elemental composition and crystal structure of the layers. Chapter 2 outlines the general experimental procedure used to fabricate the samples and the techniques used to characterize their composition, structure, and mechanical properties. Chapter 3 presents an experimental work done to prove the improvement in hardness in amorphous-crystalline multilayered systems when the intermediate layer is HCP instead of FCC. Amorphous CuTi- Crystalline Ti was used as a model system to investigate the effect of changing the intermediate layer (from FCC Cu to HCP Ti) on the mechanical properties of such systems. Chapter 4 presents an investigation of wear and scratch resistance of amorphous-crystalline multilayered systems of various thicknesses. Adhesion and wear resistance of a model system (CuZr) was investigated using adhesion scratch test. Chapter 5 presents a general conclusion and gives suggestions for future studies.

1.1. METALLIC GLASSES

Crystalline materials are made up of a number of grains of various sizes. These grains introduce crystallinity defects to the structure such as grain boundaries and dislocations. Plastic deformation happens when a sufficient load is applied to cause these dislocations to move, and generally this load is much smaller than the load that is needed to separate atomic planes by demolishing the interatomic bonds. When grains are small enough, grain boundaries become a significant portion of the material and dominate the deformation mechanism. It takes even a smaller load to deform a material along its grain boundaries, since the boundaries can slide. Grain boundaries put the material at another disadvantage as they assist chemical reactions (such as oxidation) and corrosion. Consequently, mechanical properties of a crystalline material are highly tied to its crystallographic structure. Dislocation theory is widely accepted as a simplified description of the relation between the crystal structure and the strength and ductility of a crystalline material [13].

In amorphous materials, atoms are packed in a random fashion and therefore amorphous materials do not suffer the limitations of crystalline materials. Metallic glasses, otherwise known as amorphous metals, lack the long range order that is present in crystalline materials, thus they have higher strength and hardness [2]. This random atomic packing combined with their metastable state lead to unique structural and mechanical properties [14].

The first amorphous alloy was deposited as a thin film in 1960 [15]. The crystal nucleation and growth were impeded kinetically resulting in an amorphous solid metal. In other words, rapid cooling was needed to prevent crystals from forming. This limited the fabrication to foils, ribbons, and powders. Metallic glasses with lower critical cooling rates were later discovered in 1990, thus enabling the fabrication of samples thicker than few millimeters [16]. Later on, MGs were commercialized [17] and several other MGs were developed and researched [1].

Bulk MGs have many unique properties such as high strength to weight ratio, high hardness and elastic modulus, low coefficient of friction, high scratch resistance, and high corrosion resistance [7,18,19]. Bulk MGs have been utilized to manufacture many products, such as: sports equipment, watches, electromagnetic casings, optical equipment, decorative products, choke coils, power inductors, magnetic field detection devices, shielding sheets against electromagnetic waves, medical instruments, thin film coatings, motor parts, and pressure sensors [2]. Despite the huge amounts of local plastic deformation at the shear bands, the macro plastic deformation is still limited [20], and therefore the engineering application of MGs also remained limited.

MGs were proven to lack any kind of a homogeneous plastic deformation without dislocation-mediated crystallographic slip [14,21]. A lot of research have been devoted to explain the deformation of MGs, and it was recently summarized as a series of six events [22]. The first event is STZs nucleation where atoms try to arrange themselves according the the shear strain applied. The second is the shear bands growth and propagation [23]. The third is an adiabatic heating that happens in the locally strained regions [24]. The fourth is the nucleation of nanocrtallites within or close to the existing shear bands [25]. The fifth is the generation of nanovoids in the existing shear bands [21]. And the sixth is the marry-up of the voids making even larger voids and ultimately causing fracture [26].

Another model that might also explain the deformation mechanism of MGs is the free volume model, which represents the inhomogeneous deformation in MGs as an outcome the biased accumulation of free volumes at the locations that are subjected to stress [27]. Figure 1a illustrates the atomic jump in the free volume model, while figures 1b and c illustrate the STZs model.

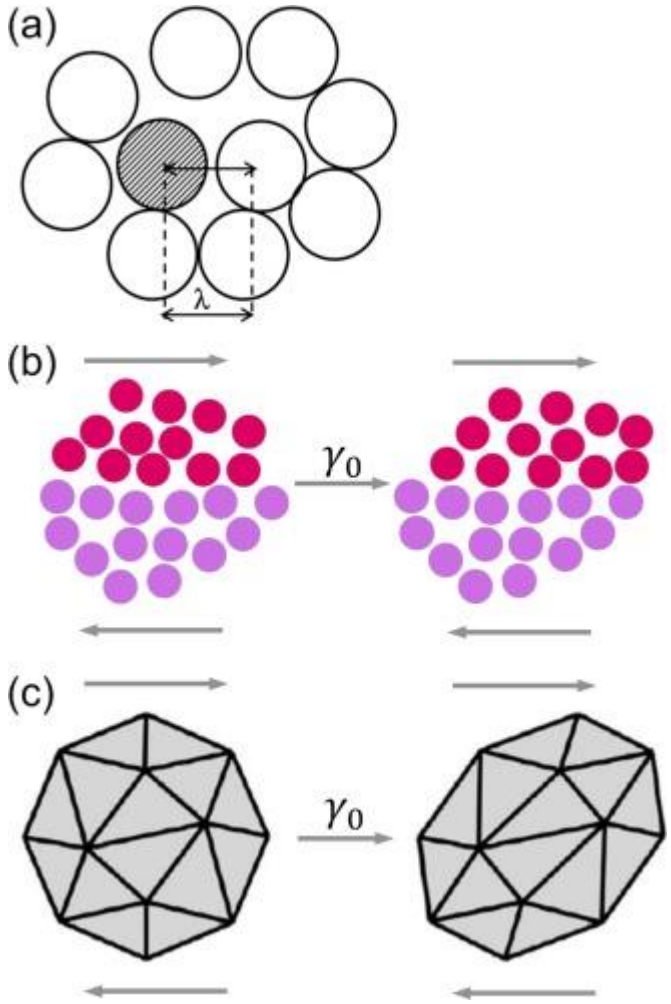

Figure 1. (a) Schematic illustration of an individual atomic jump in the free-volume model, where an atom experiences a reduced activation energy barrier when jumping to the nearest free-volume site [27]. (b) In the STZ model, dozens of atoms shear collectively under an applied shear stress [28]. (c) Idealized illustration of the STZ process when atoms are projected on a continuum mesh [29].

1.2. NANOLAYERED METALS

Mechanical properties of nanolayered metals have been widely investigated in the last two decades. Outstanding strength [30], thermal stability [31], and radiation resistance [32] of these structures make them promising engineering materials. In addition, metallic nanolayers provide a controlled and systematic approach to probing mechanical behavior of materials and interfaces at the nanoscale [33]. Especially, the nanolayers prepared by physical vapor deposition enables the precise control of layer thicknesses and provide a sharp interface to study interface dominated plastic behavior [34].

Earlier studies in the field have focused on crystalline/crystalline nanolayers (will be referred to as C/C nanolayers). The strength values of C/C nanolayers are usually much higher than the strength of its constituents. This high strength and its increase with decreasing layer thickness can be explained by the Hall-Petch behavior for layer thicknesses down to ~100 nm. For thinner layers, dislocation pile-up is no longer the dominant phenomenon, and the strengthening trend deviates from the Hall-Petch behavior. In this regime, the strength can be modeled by confined layer slip [35], by taking into account some additional factors such as interface stress and dislocation core spread [36].

The concept of nanolayered metals has recently been applied to amorphous/crystalline (A/C) nanolayers, where one of the constituent layers is a metallic glass. Outstanding ductility can be achieved by utilizing A/C nanolayers by using metallic glass constituents that are brittle in bulk form [9,37]. The presence of crystalline layers effectively hinders the catastrophic propagation of shear bands in the amorphous layers and prevent brittle failure, especially when the layer thickness is comparable to the length scale necessary for shear localization [9]. Compatibility of the flow strengths of the amorphous and crystalline layers was shown to promote codeformation, which also improves the ductility of the nanocomposite [11,37].

The strength of A/C nanolayers tend to lie in between those of the constituents, and an increase in strength with decreasing layer thickness is a common observation [12,38]. Figure 2 shows the Predominant deformation mechanisms in laminated A/B composites: dislocation pile-up, confined layer slip, and interface crossing, with respect to layer thickness. Arrows indicate the motion direction of dislocations [33].

In most studies, the flow stress of the crystalline layer is lower than the metallic glass layer, and as a result, the strength and size effects are dominated by the response of the crystalline layers. Interestingly, the application of the confined layer slip model to the softer crystalline layers predicts the strength of these composites well [12]. So far the studies focusing on the size effect on A/C nanolayers have focused on FCC crystalline layers with a large number of slip planes and relatively lower strength when compared to the amorphous layer [10,12,38]. However, there has been no study to date investigating the size effect of amorphous/HCP crystalline nanolayers (A/HCP). Recent studies in C/C nanolayers with HCP/BCC configuration have demonstrated that the geometric strengthening due to the limited number of slip planes can result in anomalous strengthening [39,40]. Therefore, A/HCP nanolayers can serve as an effective model system to gain further insight into the mechanical behavior of metallic glasses and HCP metals in confined geometries.

Flow strength can be defined as the needed stress for continuous nucleation, proliferation, and motion of plastic deformation carriers, including but not limited to twins, dislocations, and STZs, at a defined strain rate [33]. Figure 3 shows the maximum strength of nanolaminated materials with respect to the combination of constituent phases. Figure 3a shows the metal–metal crystalline laminates, figure 3b shows the metal-crystalline hard phase laminates, and figure 3c shows the metal-metallic glass laminates. Black squares indicate the strength of constituent 1 under the black line, red circles represent that of constituent 2 above the black line in the horizontal axis, and blue triangles represent that of nanolaminated composites [33].

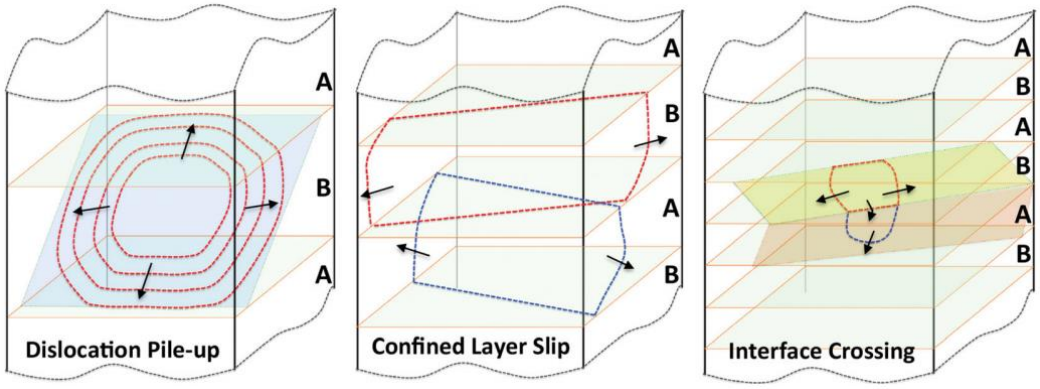

Figure 2. Predominant deformation mechanisms in laminated A/B composites: dislocation pile-up, confined layer slip, and interface crossing, with respect to layer thickness. Arrows indicate the motion direction of dislocations [33].

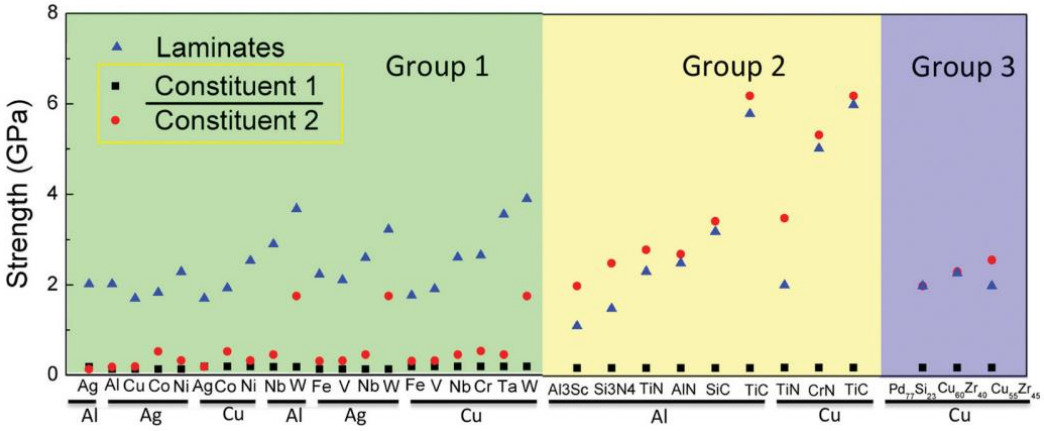

Figure 3. Maximum strength of nanolaminated materials with respect to the combination of constituent phases: (Group 1) metal–metal crystalline laminates (Group 2) metal-crystalline hard phase laminates, and (Group 3) metal-metallic glass laminates. Black squares indicate the strength of constituent 1 under the black line and red circles represent the strength of constituent 2 above the black line in the horizontal axis. Blue triangles represent the strength of nanolaminated composites [33].

1.3. PHYSICAL VAPOR DEPOSITION

One of the most common techniques used to prepare thin films is physical vapor deposition (PVD) [41]. A target material is evaporated into a vacuum chamber where the substrate is placed. Nanostructured materials in the form of thin films can be fabricated using this technique.

Magnetron sputtering is the most commonly used PVD technique for research purposes. This technique relies on magnetically accelerated inert gas ions (generally Ar^+) to knock out atoms of a target material, sputter them into a vacuum chamber, and causes them to eventually condense onto a substrate [42]. The ion bombardment of the surface of the target material generates secondary electrons which in turn results in a continuous plasma in the chamber. Figure 4 shows the mechanism of magnetron sputtering.

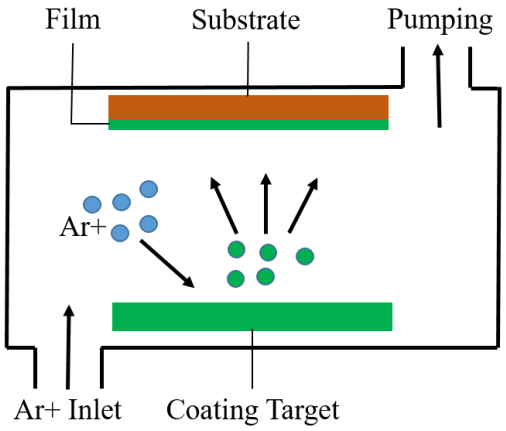

Figure 4. Magnetron Sputtering.

Two sputtering guns can be mounted to the chamber to allow the deposition of two different materials at the same time.

1.4. MICROMECHANICAL CHARACTERIZATION TECHNIQUES

Recent developments in the field of micromechanical testing have made measuring the mechanical properties of a nanomaterial possible. Micromechanical properties such as the hardness, elastic modulus, strength, adhesion, and wear resistance have all been reported in the literature [43–45]. In this section, the micromechanical characterization techniques that are used in the thesis work are reviewed.

1.4.1. NANOINDENTATION

Nanoindentation test is by far the most commonly used test to determine the hardness of materials at the nanoscale [43–45]. Nanoindentation utilizes a diamond tip which is forced into the surface of a material in order to penetrate the surface and make an impression [46]. A nanoindentation device equipped with force and displacement sensors generated the load-displacement curve of the test. The hardness is then calculated as the force applied divided by the projected area of the contact surface between the tip and the sample. Figure 5 shows the schematic of a typical load-displacement curve.

In addition to measuring hardness and elastic modulus, nanoindentation can be used to estimate the yield strength of a material [47]. Some of the drawbacks of nanoindentation have been reported in the literature such as a substrate, pile-up, and sink-in effects [48].

Nanoindentation hardness of a material is defined as [46]:

$$H = \frac{P_{max}}{A_p} \tag{2}$$

where H is the hardness, P_{max} is the maximum load during indentation, and A_p is the projected contact area between the indenter tip and the sample at maximum load. The nanoindenter measures P_{max} directly, however it is not trivial to calculate the contact area, A_p. For the calculation of A_p the well-established Oliver-Pharr method was used [46]. The full details of this method is available in the literature [46], and here the procedure is outlined. The first step in the method is the calculation of the contact stiffness, S, of the indent at the point of maximum load. For this purpose, a power-law curve fit was performed on the unloading segment of the force-displacement curve in the form:

$$P = A(h - h_f)^m \tag{3}$$

where, P is load as a function of h, which is the displacement into surface. h_f is the x-intercept of the unloading curve, as labeled in Figure 5.

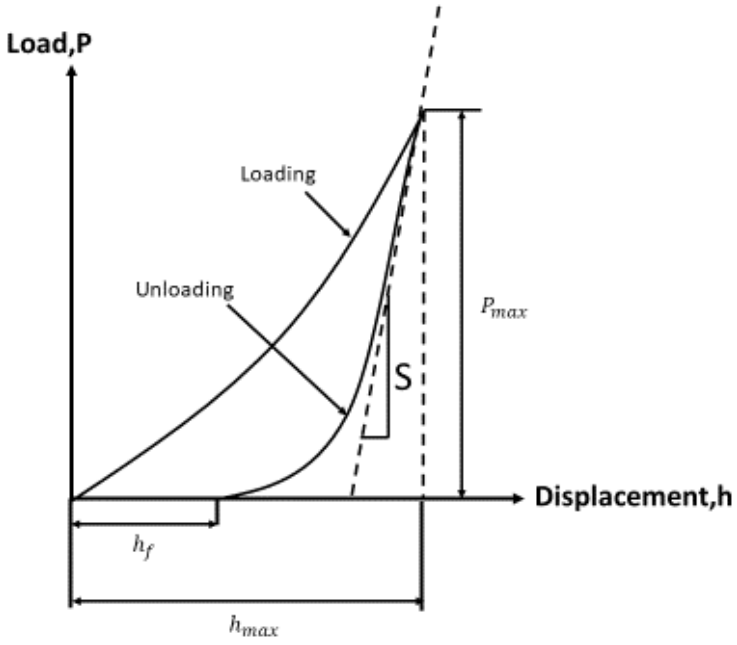

Figure 5. The schematic of a load-displacement curve for indentation [46].

Then the contact stiffness corresponds to $S = dP / dh$ calculated at h_{max}, where h_{max} is the maximum displacement into sample. Once stiffness is found, the next step is the calculation of the contact depth, h_c. If one considers a three dimensional surface as the collection of points where the tip and the sample touches each other, the contact depth is the height of this surface along the sample surface normal. Contact depth can be determined by utilizing Sneddon's expression (15):

$$h_c = h_{max} - \epsilon \frac{P_{max}}{S} \tag{4}$$

where for axisymmetric indenters, epsilon is defined as (15):

$$\epsilon = \frac{2}{\pi}(\pi - 2) \tag{5}$$

There is a direct relationship between the contact depth of the indenter and the projected area of the contact, defined by the geometry of the indenter itself. For our case, it is identical to that of a Berkovich tip, defined as:

$$A_p = 24.5 h_c^2 \tag{6}$$

The area A_p is the projected area in Equation (2), that was the last missing information for the calculation of the hardness.

1.4.2. MICRO AND NANOSCRATCH

Micro and Nanoscratch tests are similar to the macro ones but at a smaller scale. There are two types of the scratch test; scratch hardness test, and scratch adhesion test. In this section, we will focus on the scratch adhesion tests, but a brief explanation of the scratch hardness test will also be given.

Most of the information in this section has been extracted from ASTM Standard G171 [49] and ASTM Standard G1624 [50] then modified to fit for thin films scratch testing.

The scratch hardness test of a thin film is done by scratching the film with a diamond stylus (of known conical angle and tip radius) along a predetermined path. The normal force applied and the scratching speed should be defined in advance and remain constant throughout the test. To measure the size of the scratch, the width of the scratch is used as an indicative parameter of the scratch's size. An average width is measured, usually using an optical device, and the width value is used to calculate the scratch hardness of the film.

The aim of the test is to investigate the mechanical behavior of the thin film subjected to a destructive scratching and normal forces. This provides an understanding of the wear and abrasion resistance of the film. Observation within this scope is mainly deformation and damage features. The main observation is the scratch width, as it is related to the scratch hardness number. Since the scratch hardness test is only valid when there is no gross damage, deformation should only take place through the thickness of the film. These deformation features include Chevron cracks, arc tensile cracks, Hertz cracks, and conformal cracking. However, chipping and spallation are indicators of the invalidity of the scratch hardness test as they are considered as gross damage. Some of the expected through-thickness failure modes are presented in Figure 6.

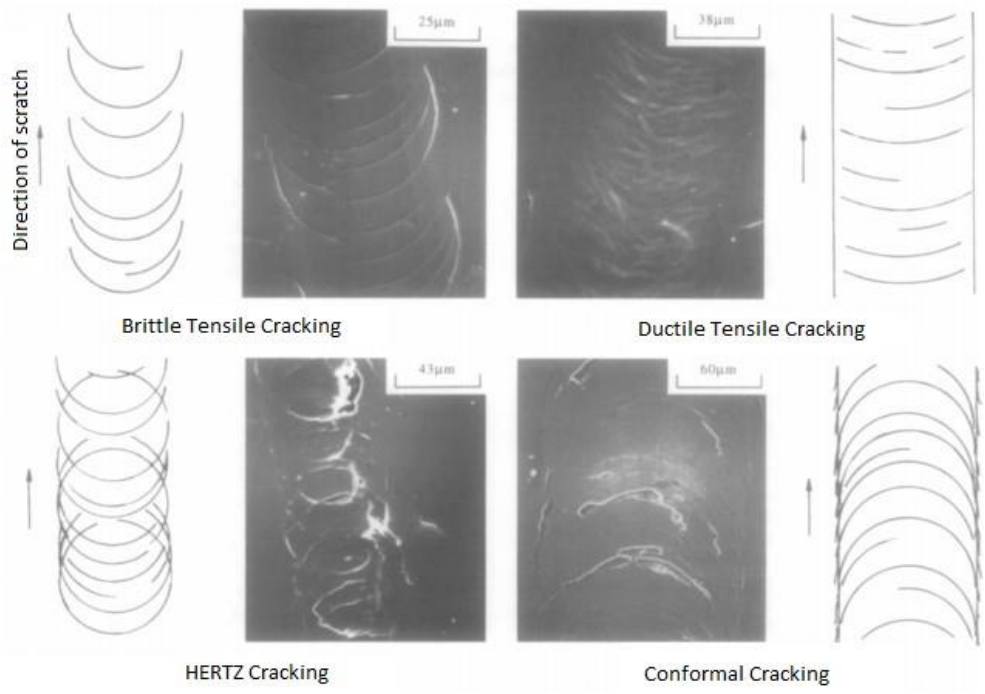

Figure 6. Through-Thickness Failure Modes [49].

These include Brittle Tensile Cracking, Hertz Cracking, Conformal Cracking, Buckling, Wedging, Recovery, and Gross Spallation. Any resulted cracks or other defects should also be reported. Microcracks, chips, and other features might be observed, and it is useful to report them.

The scratch hardness number is considered invalid in the case of large damage (such as the formation of big chips and spalls) even when the measurements were done on the unspalled section only.

The scratch adhesion test of a thin film is done by scratching the film with a diamond stylus (indenter) of known conical angle and tip radius along a predetermined path. Load during the test should increase stepwise or continuously until failure. The load at a predefined failure event is known as the critical load. In case the failure is due to delamination of the coating from the substrate, then the critical load would represent a qualitative measure of thin film adhesion.

In case the failure is of other modes such as a fracture happening within the coating (which depends on the plastic deformation within the film), then the critical load would represent a qualitative measure of the coating quality. It is not always easy to identify the critical load as it is often a range of load values and not a single load value.

The main measure in this test is the critical load at which failure occurs (detachment of the film from the substrate). Since the test is mainly used and most useful for hard coatings on hard substrates, then the expected failure spallation and buckling. When such failure modes are observed, the load is recorded and termed as the critical load. Comparison of coatings adhesion based on the critical load is possible only if the failure mechanism is the same in the samples.

The failure mode in the scratch adhesion test is highly influenced by the test load, the coating thickness, the residual stress in the coating and the properties of the substrate (e.g. hardness) as well as on test parameters such as indenter radius and sliding speed. Changing any of these parameters would alter the failure mode and prohibit the comparison of several specimens.

Lots of observations are expected, however, there are four observations that are the most meaningful. These are buckling, buckle spallation, wedging spallation, and recovery spallation. These failure modes can be seen in Figure 7. When the coating is relatively soft with a thickness of a maximum of 10 μm (for most films), buckling of the film is expected. Buckling happens due to the compressive stresses that might be generated ahead of the scratching stylus where localized interfacial defects are present to enable the buckling. When the interfacial cracks would propagate, buckling will spread laterally.

Thus curved cracks extending to the edges of or beyond the scratch track mean that the coating must have buckled. When through-thickness cracks occur in the high tensile regions within the coating, buckle spallation accumulate perpendicular to the scratch direction. The pile-up presents ahead of the stylus would enhance the failure. That is, the more pile-up accumulates in front of the tip, the more severe the failure is. Since the stylus will continue to scratch forward, it will crush the already failed region of the coating. This might lead to the partial or total removal of the failed coating. Hence, the disappearance of the failure is possible. Stages of buckling can be seen in Figure 8.

When the coating is thick enough and does not buckle, a different failure mode is expected. The high stiffness of the thicker coating would reduce the stresses in the regions ahead of the stylus. In this case, compressive cracks would form through the thickness of the film before the interfacial failure occurs. The sloping sides of the cracks would then develop tensile cracks. Since the stylus will continue to scratch forward, it will force the wedges of adjacent coating towards the empty area under the segment bound by the shear crack, thus leading to the detachment of the coating of the substrate. If the displacement is large enough, it would generate spallation ahead of the stylus. The main stages of wedging are illustrated in figure 8.

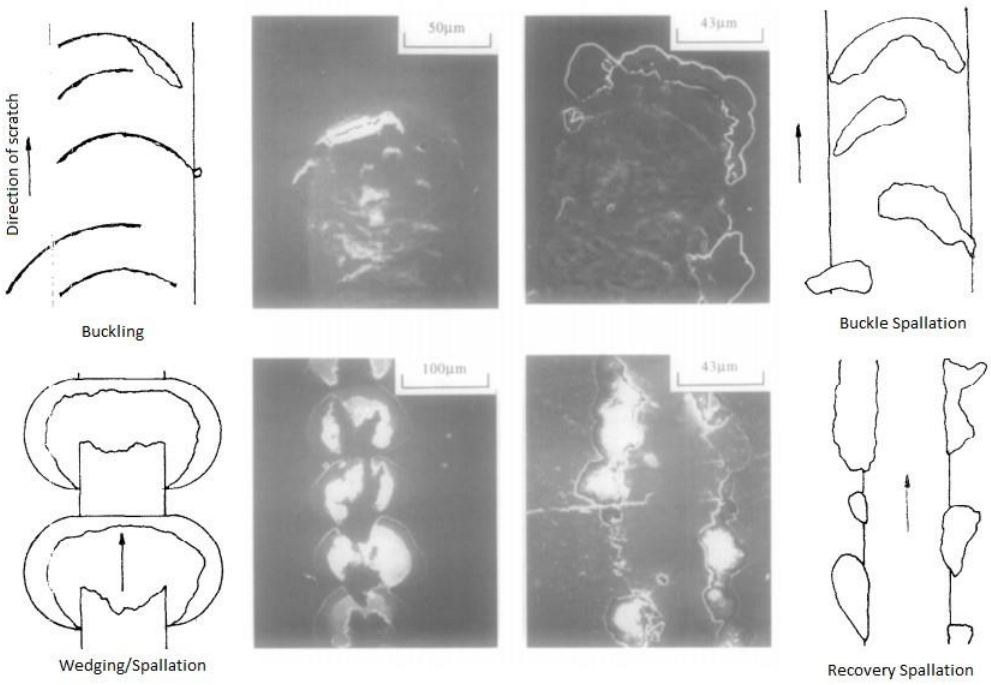

Figure 7. Interfacial Failure Modes [50].

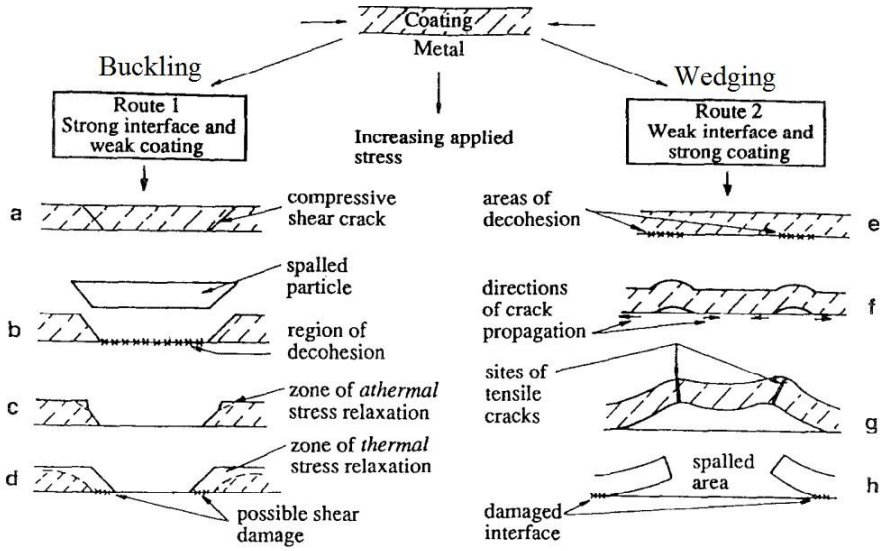

Figure 8. Buckling and Wedging Failures' Stages [50].

Table 1. Failure Modes for Different oating and Substrate Hardness [50].

Coating Hardness	Substrate Hardness	Failure Mode
Soft Coating	Soft Substrate	Plastic deformation of coating and substrate produces tensile and conformal cracking with buckling failure
Soft Coating	Hard Substrate	Plastic deformation and conformal cracking, followed by spallation and buckling failure in the coating as substrate cracks
Hard Coating	Soft Substrate	Tensile and Hertzian cracks progressing to chipping and spallation of the coating as the substrate is deformed
Hard Coating	Hard Substrate	Tensile crack followed by chipping and spallation of coating

In case the indenter falls into a hole where the coating has been removed, a dramatic increase in scratch width and scratch depth would be observed.

After the stylus passes, recovery spallation might happen behind the coating. This failure is basically the elastic recovery that happens after the deformation. Through-thickness cracking and plastic deformation of the coating are the main factors that affect the recovery spallation. Image and drawing of the recovery spallation can be seen in figure 7. Some mechanical residual stresses are expected to remain after the incomplete relaxation of the substrate since elastic deformations might be relaxed whereas plastic deformation cannot and that makes the scratch track.

The residual strain on through-thickness cracks can sometimes be totally relaxed. Tensile recovery stresses would be converted into shear stresses and directed to the nearest coating-substrate interface. Propagation of shear cracks will cause spallation on the sides of the scratch track. Such a failure mode is not likely to occur if the adhesion is good.

It is important to note the failure associated with each critical load. Based on the failure modes noted, one can decide whether or not critical load results from different scratches are comparable. In some cases, more than one failure mode might be observed on one scratch (especially if the load and thickness are near the edge of transition between two modes). In this case, both modes should be reported.

In an Acoustic Emission profile, buckling would cause a small increase, while wedging would cause a more dramatic increase. Thus reporting AE should be for the purpose of confirming the visual results and not to substitute them.

CHAPTER 2

2. EXPERIMENTAL PROCEDURES

2.1. SAMPLE PREPARATION

In this work, a VAKSİS magnetron sputterer equipped two guns (RF and DC) was used to coat all the films. Figure 9 shows the sputterer used in this thesis. 3 sets of films have been prepared, each set represents a selected model system from the literature.

Three sets of multilayered films were prepared. The first two sets are Amorphous CuTi – crystalline Cu and Amorphous CuTi – crystalline Ti. Both were sputtered on SiO2 wafers. Cu was sputtered using the RF gun while Ti was sputtered using the DC gun. All layers within the same film had the same thickness. The layer thickness was varied and several films were coated. These samples will be discussed more in Chapter 3.

The third set of multilayered films is Amorphous CuZr – crystalline Zr multilayers with various layer thickness were coated on 316L stainless steel substrates. All layers within the same film had the same thickness. The layer thickness was varied and several films were coated. These samples will be used and discussed in more detail in Chapter 4.

The total film thickness was 1 μm in all the films.

Figure 9. VAKSİS Magnetron Sputterer.

The thickness of the samples was checked by both optical profilometry and focused ion beam milling techniques. A vacuum compatible tape was used to create an uncoated region on each sample. Only one interface was used to determine the thickness profile of the film. A profilometer scanned the samples from left to right with 5 mm intervals. Figure 10 shows how the tape was applied and the interface used for profilometry.

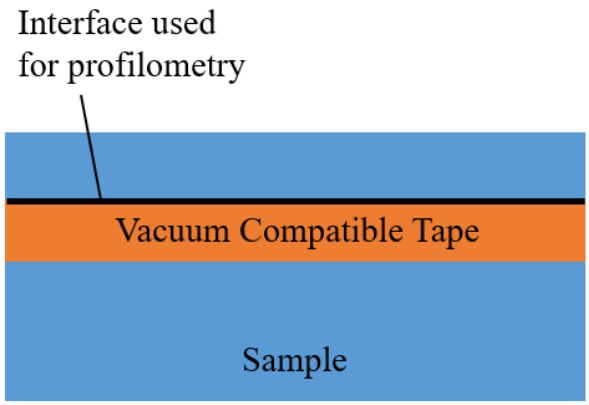

Figure 10. The interface used for profilometry.

Focus Ion Beam milling technique was used to dig into the samples and obtain scanning electron microscopy (SEM) images (see 2.3.2. for details on SEM). The images were used to measure the total thickness of the film as well as that of individual layers.

2.2. MICROSTRUCTURAL CHARACTERIZATION

In order to characterize the composition and microstructure of the samples, several characterization techniques were used. These techniques are mainly X-Ray Diffraction, Scanning Electron Microscopy, Energy-Dispersive X-ray Spectroscopy, Wavelength-Dispersive X-ray Spectroscopy, Focused Ion Beam, Transmission Electron Microscopy, and Atomic Force Microscopy. Each of these will be briefly explained in this section.

2.2.1. X-RAY DIFFRACTION

X-ray diffraction measurements are performed to characterize the microstructure of the films mainly in terms of crystallography and grain size. XRD technique works by sending an incident X-ray that interacts with the atomic planes of a material and is then diffracted with the same angle of incidence, theta.

The intensity of the diffracted rays is then measured by the instrument. Angles of maximum intensity that show up in the diffractogram refer to the crystallographic planes. The interplanar spacing (d) can then be easily calculated using Bragg's Law.

$$n\lambda = 2d_{hkl}sin\theta \quad (4)$$

Where *d* is the interplanar spacing, λ is the wavelength of the X-Ray used, and *n* is the order of the diffraction. *hkl* denotes the crystallographic directions of the atomic planes present in the film.

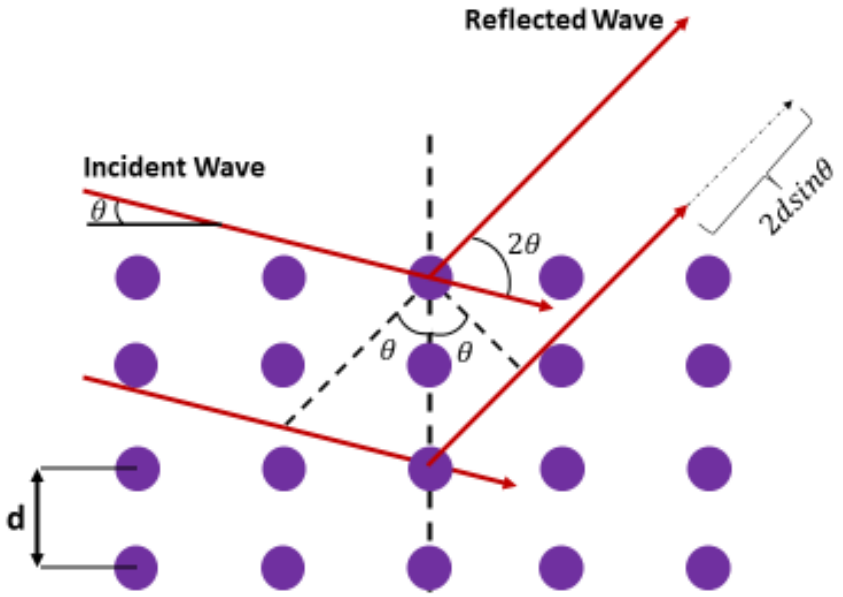

Figure 11. Bragg's Law illustration [51].

Scherrer Equation can be then used to approximate the crystal size by relating the peak width (*B*) and crystallite size (*L*):

$$L = \frac{K\lambda}{B(2\theta)cos\theta} \tag{5}$$

Where *K* is a dimensionless value representing the shape factor and *B* is the full width of the associated diffraction peak at half maximum (*FWHM*). 89 - 0.94 are acceptable values for *K* [51], we used 0.9 in our approximation.The expression shows that wider peaks belong to smaller crystallites. A detailed explanation of the technique and the calculation have been documented in the literature [52]. A Rigaku Ultima-IV diffractometer was used to perform the XRD measurements on all the films in grazing incidence mode at 1°. Scherrer equation was applied by Jade MDI software to approximate the average crystal size in the films. The wavelength used by the machine is that of copper wavelength i.e. ($K\alpha$) is 1.5418 Å at 22.85°C.

2.2.2. SCANNING ELECTRON MICROSCOPY AND ENERGY-DISPERSIVE X-RAY SPECTROSCOPY

Scanning electron microscopy is one of the most commonly used techniques to look closely at samples with microscale features. SEM works by sending a focused electron beam at a spot of a sample and collecting all the electron that result from the interaction with the surface of the sample; these electrons carry a lot of information about the composition and the topography of the scanned sample [53]. Energy-Dispersive X-ray Spectroscopy is a technique used within the scope of SEM but works by collecting the resulting X-ray from the interaction with the surface. In our work FEI Quanta 400F scanning electron microscope (SEM) performed surface imaging and EDS. Figure 12 shows the signals that result from the interaction between the incident electron beam and the sample's surface.

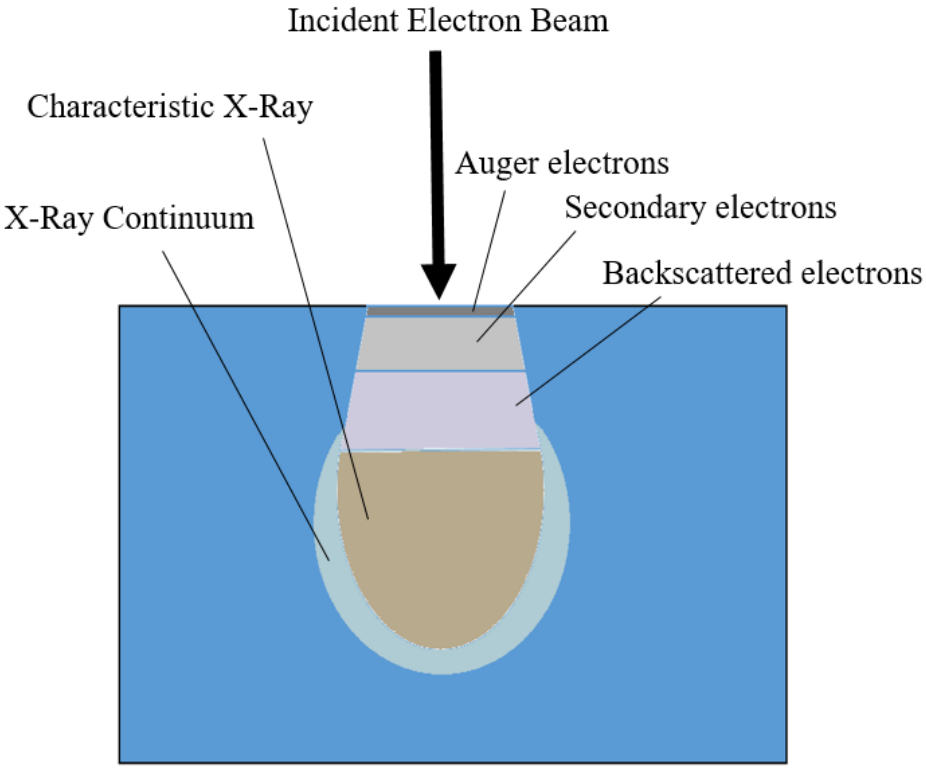

Figure 12. The interaction between the incident electron beam and the sample's surface

2.2.3. FOCUSED ION BEAM

Focused Ion Beam milling is a technique that is widely used in order to machine parts at the micro and even nanoscale. TEM samples and SEM cross-sections were prepared using this technique. An FEI Nova 600 Nanolab focused ion beam (FIB) was used in this work. This system can do FIB and SEM simultaneously. Figure 13 shows an illustration of the system.

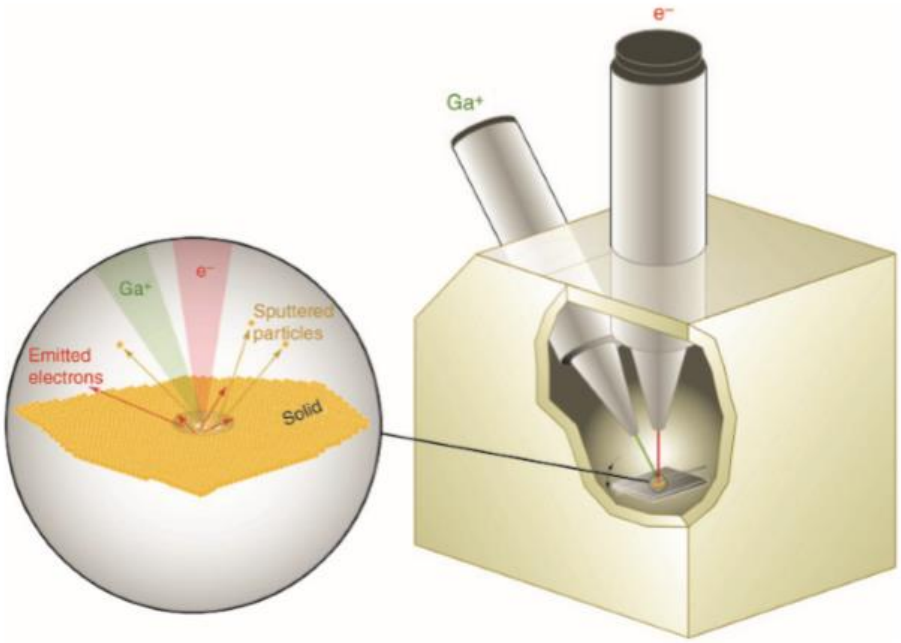

Figure 13. Illustration of FIB and SEM dual system [54].

The samples are first coated with platinum to protect the surface from any damage. The sample is then milled into the desired shape by focusing positive Gallium ions on the surface.

2.2.4. TRANSMISSION ELECTRON MICROSCOPY

Transmission electron microscopy is a technique that uses a beam of electrons to penetrate a sample that 100 nm thick or thinner to generate an image using the transmitted electrons. The image is then enlarged and sent to a camera or to a fluorescent screen. This technique allows imaging of very small objects and can be image individual atoms. The device used to perform the TEM microscopy in this work is Jeol JEM2100F Field Emission Transmission Electron Microscope. A Nova 600 Nanolab focused ion beam (FEI Company, OR, USA) prepared the TEM samples using the lift-out technique (see section 2.2.3).

2.2.5. ATOMIC FORCE MICROSCOPY

Atomic force microscopy is another technique to image the topography of the sample. It can also show individual grains with sizes down the atomic scale. In this work, AFM was used to scan the cross-section profiles of the scratch tests and to measure the surface roughness of the 316L stainless steel substrates.

2.3. MECHANICAL CHARACTERIZATION

As mentioned before, micromechanical testing has made measuring the mechanical properties of a nanomaterial possible. Micromechanical properties such as the hardness, elastic modulus, strength, adhesion, and wear resistance have all been reported in the literature [43–45] and are used in this work. In this section, the devices used to perform micromechanical characterization techniques in the thesis work are reviewed.

2.3.1. NANOINDENTATION

Nanoindentation technique (introduced in section 1.3.1.) was used to probe the hardness and elastic modulus values of all the films. An Agilent G200 nanoindenter measured the hardness of the films by using a Berkovich tip in continuous stiffness measurement mode [55]. Nanosuite software was used to analyze the data, and hardness and elastic modulus data were obtained from a depth of around 200 nm into the surface.

2.3.2. NANOSCRATCH

The same nanoindenter performed the nanoscratch tests in ramping load mode. A conical diamond tip with 5 μm radius and an included angle of 90° was used. The normal force increased linearly from 0 mN to 500 mN over a total scratch length of 500 μm. The scratch speed was 40 μm/s, resulting in a loading rate of 40 mN/s and 1 mN/μm. Before each test, the scratch path was scanned with a very low load of 50 μN to compensate for any slope or irregularity on the surface. The penetration depth vs. scratch length profiles show the average of 10 scratches for each sample, separated by at least 75 μm, which is larger than seven times the diameter of the indenter tip.

CHAPTER 3

3. SIZE INDEPENDENT STRENGTH OF AMORPHOUS – HCP CRYSTALLINE METALLIC NANOLAYERS

This chapter is reproduced with permission from Mohammad Abboud and Sezer Özerinç, "Size independent strength of amorphous – HCP crystalline metallic nanolayers", submitted to JMR, 2018 [56].

3.1. INTRODUCTION

In this work, we experimentally investigated the structure-property relationships in CuZr/Zr and CuTi/Ti A/C nanolayers. CuTi/Cu nanolayers were also considered for comparison purposes. The microstructural investigations combined with nanoindentation hardness provided insight into the size-independent strength of A/HCP nanocomposites and the results were interpreted by utilizing the confined layer slip model.

Amorphous/crystalline (A/C) nanolayers provide an effective model system to study the mechanical behavior and size effects of metallic glasses and crystalline metals in confined geometries. In this work, we experimentally investigated the structure-property relationship in A/C nanolayers containing HCP crystalline layers. CuTi/Ti and CuZr/Zr nanolayers were prepared by magnetron sputtering with layer thicknesses in the range 10–100 nm. The hardness of the CuTi/Ti and CuZr/Zr nanolayers were close to those of the monolithic CuTi and CuZr, respectively.

The hardness remained virtually the same for different layer thicknesses as opposed to CuTi/Cu amorphous/FCC crystalline nanolayers which exhibit increasing strength with decreasing layer thickness. The results can be explained by the confined layer slip model that predicts an effective flow stress for HCP crystalline layers higher than those of the amorphous layers. As a result, the strength and size-effects are governed by the mechanical behavior of the softer amorphous layer.

3.2. EXPERIMENTAL DETAILS

We prepared thin film samples of pure metal, metallic glass, and A/C nanolayered composites. Pure metal samples were Zr and Ti films, and monolithic metallic glass samples had a composition of $Cu_{60}Ti_{40}$ and $Cu_{45}Zr_{55}$. Three different types of nanolayered A/C composites were prepared, namely, $Cu_{60}Ti_{40}$/Ti, $Cu_{60}Ti_{40}$/Cu, and $CuZr_{45}Zr_{55}$/Zr. Series of samples with different layer thicknesses in the range 10 – 100 nm were deposited for each case. We will refer to the monolithic metallic glass samples as CuTi and CuZr, and nanolayered samples as CuTi/Ti-X, CuTi/Cu-X and CuZr/Zr-X where X denotes the nominal thickness of the crystalline layers. Table 2 shows a list of samples prepared and their naming convention together with the measured average layer thicknesses for each case.

A magnetron sputterer (VAKSİS, Turkey) deposited the films of 1 μm nominal thickness on oxidized single crystal silicon substrates at an Ar pressure of 2.2×10^{-3} Torr. The only exception was CuZr/Zr samples, which were deposited on polished stainless steel substrates. The base pressure of the sputtering chamber was below 1×10^{-7} Torr before deposition. Sputtering targets were 2" diameter and 1/4" thickness elemental disks of 99.99% purity (Kurt J. Lesker, PA, USA). We calibrated the deposition rates by using a ZYGO 7200 optical profilometer (CT, USA). The sputtering power was adjusted to keep deposition rates at ~10 nm/min. A Quanta 400F (FEI Company, OR, USA) scanning electron microscope (SEM) equipped with an EDS detector (Oxford Instruments, UK) verified the compositions of the monolithic metallic glasses by energy-dispersive X-Ray spectroscopy (EDS).

Table 2. List of the samples prepared for this study. Naming convention uses the nominal layer thickness of the crystalline layers. Actual layer thicknesses were measured by TEM and/or SEM cross-sections.

Sample Name	Morphology	Amorphous Layer Thickness (nm)	Crystalline Layer Thickness (nm)
Cu	pure, nanocrystalline	–	1 µm monolithic
Ti			
Zr			
CuTi	$Cu_{60}Ti_{40}$	1 µm monolithic	–
CuZr	$Cu_{45}Zr_{55}$		
CuTi/Ti-75	alternating layers of $Cu_{60}Ti_{40}$ and pure Ti	74	74
CuTi/Ti-50		48	48
CuTi/Ti-25		24	24
CuTi/Ti-10		8	8
CuTi/Cu-100	alternating layers of $Cu_{60}Ti_{40}$ and pure Cu	75	105
CuTi/Cu-50		35	50
CuTi/Cu-30		21	30
CuTi/Cu-10		6	9
CuZr/Zr-100	alternating layers of $Cu_{45}Zr_{55}$ and pure Zr	95	95
CuZr/Zr-40		40	40
CuZr/Zr-10		9	9

The microstructures of the films were analyzed by X-ray diffraction (XRD) and transmission electron microscopy (TEM). An Ultima IV diffractometer (Rigaku, Japan) analyzed the samples in the glancing angle mode where the angle between the incoming beam and the sample surface was 1°. A Nova 600 Nanolab focused ion beam (FEI Company, OR, USA) prepared the TEM samples using the lift-out technique. A JEM 2100 HRTEM (JEOL, Japan) imaged the samples at 200 kV. A Gatan Model 794 Slow Scan CCD and a Gatan 833 Orius SC200D CCD Camera took the images.

An Agilent G200 nanoindenter equipped with a diamond Berkovich tip performed the indentation measurements on all samples. The measurements employed the continuous stiffness measurement mode [57]. 16 indentations were performed on each sample and the results presented are the average values.

3.3. RESULTS

3.3.1. MICROSTRUCTURE

Figure 14 shows the XRD results of all samples. Pure Cu, Ti and Zr exhibit several sharp peaks indicating their polycrystalline structure. XRD patterns of the CuTi and CuZr monolithic films show wide humps that are characteristic of a fully amorphous structure. All nanolayered films show a combination of the amorphous humps and sharp peaks as a result of the reflections from crystalline and amorphous layers combined. However, the XRD patterns of the nanolayered samples are not a direct superposition of the pure metal and the metallic glass patterns, indicating that confinement into a layered geometry changes the grain morphology and texture.

Figure 14(a) compares the CuTi/Cu nanolayers with pure crystalline Cu and CuTi metallic glass. Pure Cu shows strong reflections from (111) and (200). (111) peak has a much higher intensity, and comparing the relative intensities with those of powder diffraction data (ICDD PDF Card No. 004-0836 [58]) suggests that there exists (111) texture. Same Cu peaks are present in the patterns of CuTi/Cu, suggesting that Cu confined in the layered geometry also exhibits a similar texture. On the other hand, the peaks widen with decreasing layer thickness, suggesting grain refinement.

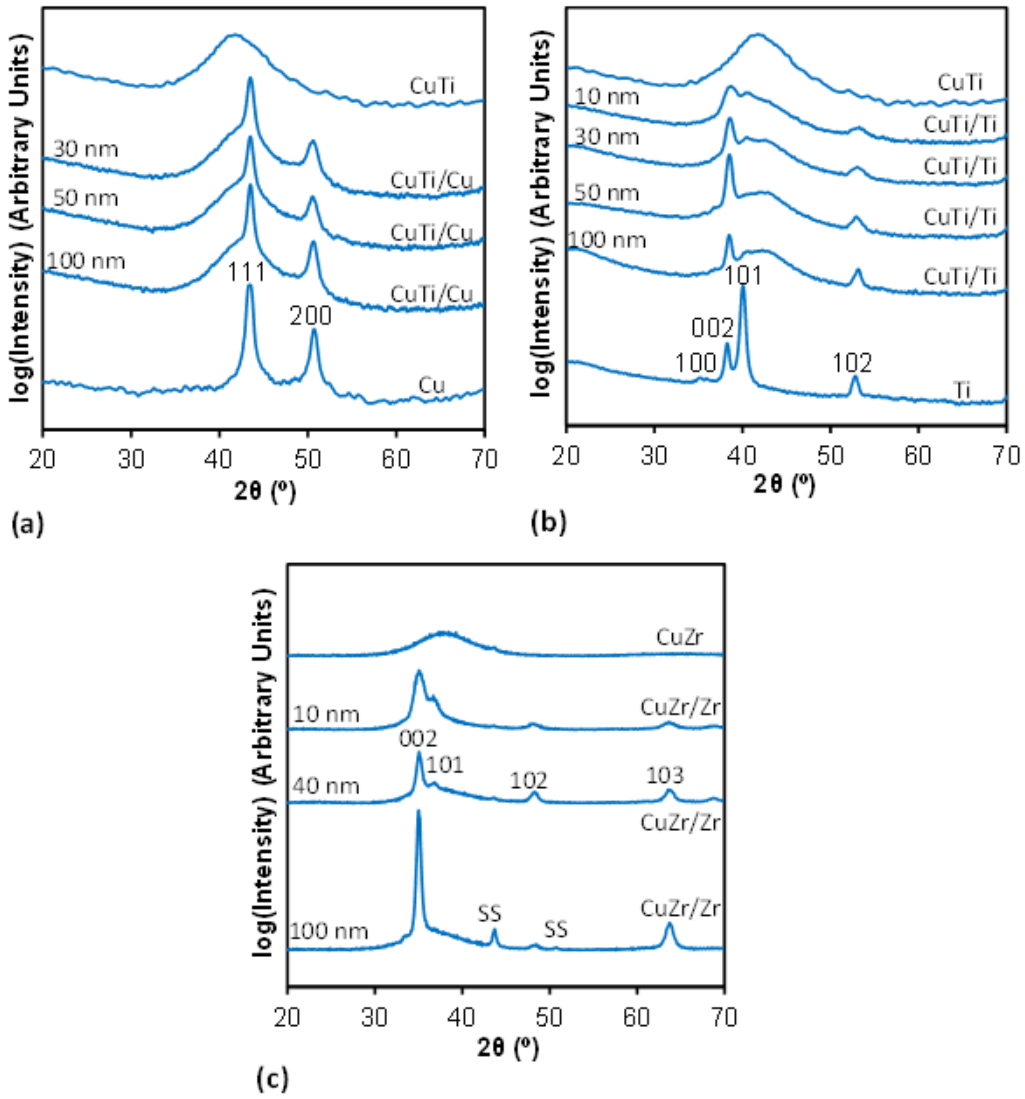

Figure 14. XRD data of (a) CuTi/Cu, (b) CuTi/Ti, and (c) CuZr/Zr nanolayers, and those of monolithic metallic glasses and pure metals. Layer thicknesses of nanolayered samples are indicated on the left of the spectra. SS refers to the stainless-steel substrate for the case of CuZr/Zr.

Figure 14(b) presents the same data for the CuTi/Ti nanolayers and pure Ti. XRD pattern of Ti indicates an HCP structure, with reflections from (101), (002) and (102) in the order of decreasing intensity. The pattern resembles that of powder diffraction (ICDD PDF Card No. 044-1294 [58]), suggesting that the grain orientations are random to a great extent. However, when it comes to nanolayered CuTi/Ti, the (101) peak almost disappears, and (002) & (102) peaks dominate. This dramatic change in the XRD pattern indicates that the confinement of Ti in a layered geometry promotes a strong texture, with the basal planes of the HCP crystals becoming mostly aligned with the interface. When the layer thickness changes from 100 nm to 50 nm, the (002) intensity increases, suggesting an increase in the texture. However, with a further decrease in the layer thickness, (002) intensity starts to decrease, and (101) peak appears again with a relatively low intensity, suggesting that the texture becomes relatively weaker.

Figure 14(c) shows the results for CuZr and CuZr/Zr samples. (002) exhibits the highest intensity in the CuZr/Zr, showing that the preferred texture in Zr is similar to that of Ti in the CuTi/Ti samples. (002) and (103) reflections become stronger with increasing layer thickness accompanied by a decrease in the intensity of (101). These trends indicate that the (002) texture is relatively stronger for the 100 nm layers when compared to the 10 nm layers.

Figure 15 shows the estimated grain sizes for all samples. The calculations utilized Scherrer equation based on (111) peaks of Cu, and (002) peaks of Ti and Zr. Grain sizes are the largest for the monolithic pure films and monotonically decrease with decreasing layer thickness, which is a trend commonly encountered in magnetron sputtered layered films [40].

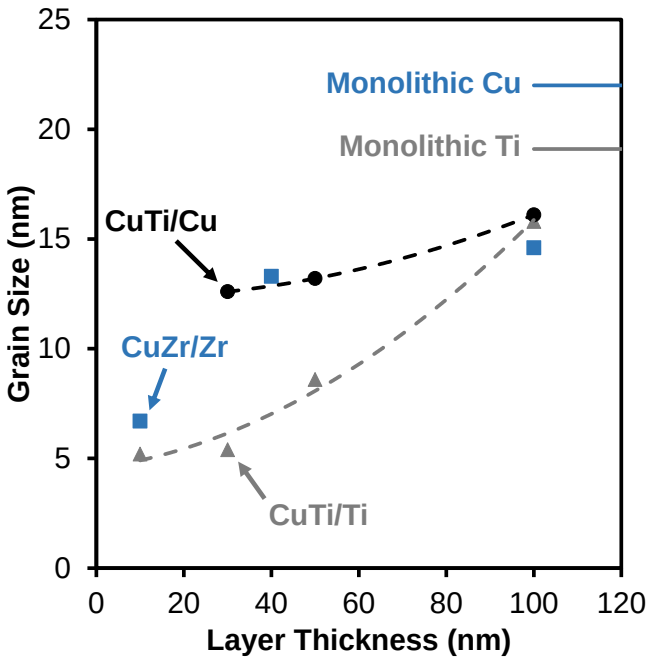

Figure 15. Grain sizes estimated from Scherrer equation using (111), (002), and (002) peaks for Cu, Ti, and Zr layers, respectively. Solid lines indicate the grain sizes of the monolithic pure films. Grain sizes are the largest for monolithic films and monotonically decrease with decreasing layer thickness.

Figure 16 shows the bright field TEM images of selected samples. Figure 16a-c shows CuTi/Cu samples with layer thicknesses of 10, 30, and 100 nm. The crystalline layers exhibit a columnar grain growth commonly encountered in sputtered films [59]. The diffraction patterns shown in the top insets are from multiple layers and indicate [111] texture perpendicular to interfaces. The crystalline and amorphous layer thicknesses are not the same, CuTi layers possess a thickness that is ~70% of those of the crystalline layers. As we will discuss in the subsequent sections, the plasticity is dominated by the crystalline layers, and we refer to these samples by the thickness of their respective crystalline layers.

Figure 16d and e show CuZr/Zr-40 and CuZr/Zr-100, with alternating layers of nanocrystalline Zr and amorphous CuZr [60]. Similar to the CuTi/Cu, columnar grain growth is observed. The top insets show diffraction patterns from areas that include multiple layers and indicate that there exists texture with [001] direction being perpendicular to the layers. The results are in agreement with the XRD patterns, where (002) reflections were pronounced.

Figures 16f shows the cross-sections of CuTi/Ti-100 sample with a more pronounced waviness. Such waviness is a consequence of the less uniform growth of the crystalline Ti layers, where a small roughness introduced at a layer propagates to subsequent layers and gets amplified with an increasing number of layers. Such waviness is occasionally encountered in magnetron sputtered nanolayers [40]. While such waviness can potentially affect the results of micropillar compression experiments [10] and interfacial shear strength measurements [61], it is less likely to alter the nanoindentation hardness response which induces a complicates stress state below the indenter. Previous studies show that the deformation of such wavy layers can be successfully modeled well by confined layer slip [40].

The second insets below the composite diffraction patterns in Figures 16b, e, and f are taken from an individual metallic glass layer, and the diffuse ring shape verifies the fully amorphous nature of the respective CuTi and CuZr layers.

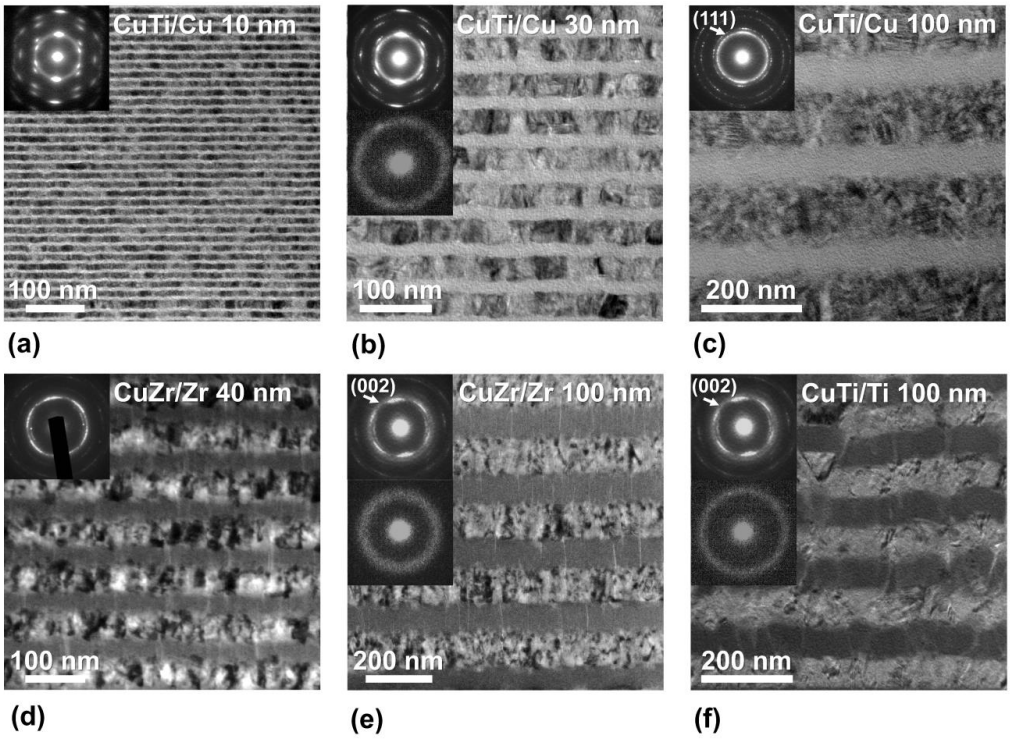

Figure 16. Bright field cross-sectional TEM images of (a) CuTi/Cu-10 (c) CuTi/Cu-30, (c) CuTi/Cu-100, (d) CuZr/Zr-40, (e) CuZr/Zr-100, and (f) CuTi/Ti-100. The insets on the top right corners show diffraction patterns taken from a region including multiple layers. The second insets below are nanodiffraction patterns corresponding to the respective amorphous layers.

3.3.2. MECHANICAL PROPERTIES

Figure 17a demonstrates example nanoindentation data for CuTi/Ti-30. The inset shows the load-displacement curves of individual indentations exhibiting very good repeatability, and the main figure shows the hardness calculated as a function of depth using continuous stiffness measurements. Figure 17b summarizes the average hardness and elastic modulus measurements of all samples. The average hardness and elastic modulus values were taken at a depth of ~200 nm into the films where the data show a plateau indicative of the zone least affected from the tip imperfection and substrate effects. Results of pure metal and monolithic metallic glass samples are shown by dashed lines whereas markers indicate the properties of the respective nanolayers. Pure nanocrystalline Ti, Cu, and Zr have hardness values of 2.04 ± 0.38 GPa, 2.2 ± 0.22 GPa and 7.03 ± 0.25 GPa, respectively. The hardness of CuZr metallic glass is 5.72 ± 0.16 GPa, which lies in between those of pure Cu and Zr. On the other hand, CuTi has a hardness of 7.04 ± 0.36 GPa, that is much higher than those of its constituents.

When it comes to the layered samples, there exist two different trends. CuTi/Ti and CuZr/Zr hardness values do not vary with layer thickness, whereas CuTi/Cu hardness monotonically decreases with increasing layer thickness. CuTi/Ti hardness is virtually the same as that of CuTi metallic glass, and CuZr/Zr exhibits a similar behavior with a hardness almost identical to that of CuZr metallic glass. The figure also shows CuZr/Cu data from literature [12], which shows decreasing hardness with increasing layer thickness. The layer thickness-dependent hardness behavior is very similar for our CuTi/Cu samples and for CuZr/Cu values previously reported [12].

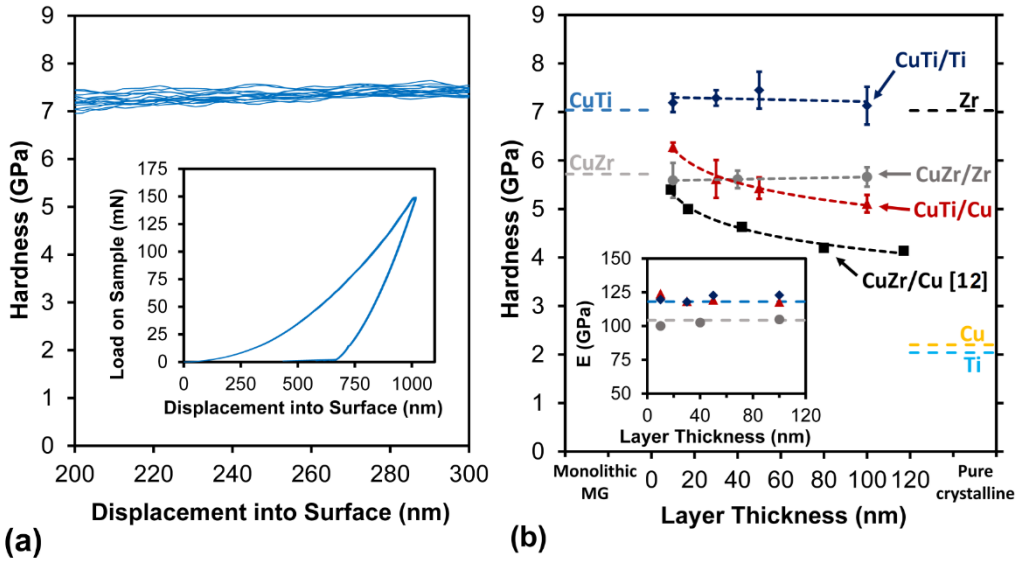

Figure 17. (a) Hardness of CuTi/Ti-30 as a function of indentation depth, as determined by the continuous stiffness measurement technique. Each curve corresponds to an individual indentation. The inset shows corresponding load-displacement data, demonstrating the repeatability of the results. (b) Average hardness of all samples as measured by nanoindentation. Dashed lines indicate the hardness of monolithic metallic glasses (MG) on the left and pure crystalline metals on the right. Inset shows the elastic modulus data of monolithic metallic glasses and nanolayered samples using the same marker and color convention used in the main figure.

The inset of Figure 17b shows the elastic modulus values of all samples. CuTi and CuZr have elastic moduli of 118.1 ± 3.9 GPa, and 104.3 ± 1.2 GPa, respectively. Elastic moduli of the layered samples are very close to those of the corresponding monolithic metallic glass films. The variation of modulus with layer thickness is within 2.0% for CuTi/Cu, 1.7% for CuTi/Ti, and 1.9% for CuZr/Zr, which are comparable to the standard deviations of the data. Table 3 summarizes the mechanical properties measured for all samples.

Table 3. Summary of hardness and elastic modulus results based on nanoindentation measurements.

Sample Name	Hardness (GPa)	σ_H (GPa)	Elastic Modulus (GPa)	σ_E (GPa)
Cu	2.2	0.22	111.6	5.8
Ti	2.04	0.38	66.44	10.27
Zr	7.03	0.25	120.6	2.9
CuTi	7.04	0.36	118.1	3.9
CuZr	5.72	0.16	104.3	1.2
CuTi/Cu-100	5.11	0.18	117.8	2.3
CuTi/Cu-50	5.43	0.22	119.4	2.7
CuTi/Cu-30	5.62	0.39	118.4	4.6
CuTi/Cu-10	5.28	0.09	124.0	1.2
CuTi/Ti-75	7.13	0.39	122.9	3.2
CuTi/Ti-50	7.45	0.38	122.7	3.1
CuTi/Ti-25	7.29	0.16	118.0	2.0
CuTi/Ti-10	7.19	0.19	119.7	1.45
CuZr/Zr-100	5.66	0.2	104.9	1.9
CuZr/Zr-40	5.61	0.18	102.6	1.2
CuZr/Zr-10	5.59	0.36	100.1	1.0

3.4. DISCUSSION

Overall, the hardness of the pure films and the monolithic metallic glasses are in agreement with the literature values. The hardness of nanocrystalline Cu was measured as 2.2 GPa, which is very close to the results reported for sputtered nanocrystalline Cu with similar texture and grain size [59]. Nanocrystalline Zr, on the other hand, usually exhibits hardness values in the range 4 – 6 GPa [62], rendering the measured 7 GPa significantly high. This high hardness can be attributed to the strong texture of the Zr films in our case. For example, the yield strength of (002) textured nanocrystalline Zr micropillars can reach 2.6 GPa [11], and using a Tabor factor of 2.7 [63], the hardness can be estimated as 7 GPa, which is in good agreement with our findings. The hardness of nanocrystalline Ti can vary in the range 1.5–6 GPa depending on the grain size, texture and impurity levels [62], and the relatively low hardness of the Ti films in this study might be due to the lack of texture.

Monolithic CuZr is one of the most frequently studied thin film metallic glasses in the literature [4], and its hardness can vary in the range 4.5 – 7.5 GPa depending on the composition [64,65]. Our results are in very good agreement with the findings of Wang et al. [64], in which hardness of $Cu_{50}Zr_{50}$ was measured as ~6 GPa. CuTi metallic glass, on the other hand, is a relatively less explored system, and the literature about its mechanical properties is quite limited. CuTi prepared by melt-spinning has a hardness of 8.5 GPa, somewhat higher than our measurements of ~7 GPa [66]. Metallic glasses prepared by vapor deposition are usually expected to be harder than their rapidly solidified counterparts, as melt-spinning results in slower cooling rates and a more ordered structure with less free volume when compared to sputtering [67]. When it comes to the nanolayered samples, CuZr/Zr and CuTi/Ti show a drastically different behavior when compared to CuTi/Cu, which provides a way of gaining insight into the deformation mechanisms involved in A/C composites.

First, the behavior of CuTi/Cu will be considered, which is mostly in agreement with the previous findings. The hardness of CuTi/Cu exhibits an increase with decreasing layer thickness, a behavior commonly observed in many C/C [68–70,36,71,40] and A/C [12,38] nanolayered systems. In C/C systems, the observed size effect down to layer thicknesses of ~100 nm is analogous to grain boundary strengthening, where the interfaces with a large number density act as obstacles to dislocation motion [68]. For layer thicknesses in the range 10-100 nm, strength continues to rise; however, the dislocation pile-up behavior that mediates the strengthening is no longer dominant, and the flow stress can be estimated through a modified confined layer slip model [36]. At a layer thickness below 10 nm, dislocations start to cross the layer interfaces, and the strength tends to reach a plateau [72]. When there is a crystallographic mismatch between the two constituent layers, the weak interface acts as a stronger barrier to dislocation motion, and this results in extraordinary strengthening such as the case of Cu/Nb with compressive strengths exceeding 2.4 GPa [30]. Since the MG layers are size independent, the critical parameter leading to the size effect is the Cu nanocrystalline layer thickness. Therefore, the layer thickness difference of Cu and CuTi is not expected to affect the result.

The plastic response of A/C nanolayers differs from those of C/C layers, as amorphous materials do not contain dislocations. In metallic glasses, the plasticity is mediated by STZ and shear bands formed by their percolation [73]. In most A/C nanolayers studied, the bulk strength of the metallic glass component is higher than that of the crystalline phase, and as a result, the softer crystalline layer yields first upon loading. When loading is perpendicular to the layers, compressive stresses develop in the crystalline layers upon deformation, as a result of their confinement in between hard amorphous layers. This compressive stress will gradually increase the effective flow stress of the crystalline layer. The dislocations terminating at the interface will eventually trigger the formation of STZs in the metallic glass layers and will promote the codeformation of all layers [33].

The strength of CuTi/Cu samples can then be interpreted by comparing the strength of monolithic CuTi and Cu, which are ~7 GPa and 2.2 GPa, respectively. As nanoindentation induced deformation corresponds to an average strain level of ~8% [74], the hardness of the nanocomposite is expected to reflect a combination of Cu that yields initially and that of CuTi that deforms subsequently. Our hardness results for CuTi/Cu and reported values for CuZr/Cu [12] lie in between the hardness values of the constituents, in agreement with this explanation.

The strengthening of CuTi/Cu with decreasing layer thickness can be attributed to the strengthening in the Cu layers, as metallic glasses do not show a strong size effect [75,76]. With decreasing layer thickness, average grain size decreases, and the number of interfaces increases, both of which increase the total volume fraction of the boundaries that impede dislocation motion in Cu. Furthermore, the disordered structure of the metallic glass layers with a high level of free volume promotes dislocation starvation at the boundaries of Cu, potentially resulting in additional strengthening. The combined effects of these are reflected in our experimental results for CuTi/Cu, where there is a monotonic increase in hardness with decreasing layer thickness.

The hardness of CuTi/Cu can be modeled by using the modified confined slip (CLS) model developed by Misra et al. [36], that takes into account the effects of dislocation core spreading, interface stress, and interactions between the arrays of dislocations. Although the model was first utilized to explain the deviations from the Hall-Petch behavior in FCC/BCC incoherent nanolayers, it has been successfully applied to a number of nanolayers [77,40,78] including A/C systems [10,12]. According to the model, the normal stress required to propagate a glide loop of Burgers vector *b* within a single Cu layer can be estimated as:

$$\sigma_{cls} = \frac{M\mu b}{8\pi(h/sin(\varphi))} ln\left(\frac{\alpha}{b_{Cu}}\frac{h}{sin(\varphi)}\right)\left(\frac{4-\upsilon}{1-\upsilon}\right) - \frac{f}{h} + \frac{\mu b}{L(1-\upsilon)} \qquad (7)$$

In this equation, M is the Taylor factor, μ is the effective shear modulus, b is the length of the Burgers vector, ν is Poisson's ratio, and h is the layer thickness. φ is the angle between the glide plane and the interface, therefore, $h/\sin(\varphi)$ gives the effective thickness of the layer along the glide plane. α is the core cutoff parameter (< 1) where smaller values indicate a wider dislocation core. f is the interface stress caused by the elastic deformation of the interface region and it assists the deformation process for compressive geometries, which is the case for nanoindentation. Finally, L is the spacing between the parallel array of glide loops. Tabor factor values were taken similar to the ones in the literature [10,12]. By using Equation (7) with a Tabor factor of 2.7, the hardness of the layers can be estimated as $H = 2.7\sigma_{cls}$.

For CuTi/Cu, considering the deformation of the Cu layers, b_{Cu} = 0.26 nm, ν = 0.34, and $\varphi = 70.5°$. α defines the extent of core spreading, and unfortunately, there is no available quantitative data for A/C interfaces. For Cu/Nb nanolayers, molecular dynamics simulations suggest an α value of 0.2 [79], while α = 0.45 predicts the literature data for CuZr/Cu layers well [12].

When it comes to the interface stress, A/C interfaces have f values approximately in the range 0.5 – 1.1 J/m^2 [80,81]. Glide loop spacing, L, is related to the strain in the layers by $\varepsilon = b / L$. The average strain in the plastically deforming region under a Berkovich indenter is ~8% [63], which corresponds to an L of ~3.2 nm. A relatively larger L value in the range 5–15 nm usually predicts the experimental results better, which can be attributed to the low strain hardening in crystalline nanolayers [69,82]. Based on these previous findings, and utilizing the parameters used for modeling CuZr/Cu nanolayers [12], Figure 18 shows the predictions of the CLS model for CuTi/Cu, using α = 0.45, f = 1.1 J/m^2, L = 5 nm, and μ = 20.3 GPa. There is a relatively good agreement between the model predictions and the experimental data for CuTi/Cu.

The higher experimental hardness values for layer thicknesses of 50 and 100 nm can be attributed to the polycrystalline structure of the layers. CuTi/Cu-50 and CuTi/Cu-100 have average grain sizes of 9 and 16 nm, respectively, and this high density of grain boundaries within the layers can act as additional obstacles to dislocation motion as predicted by molecular dynamics simulations [83].

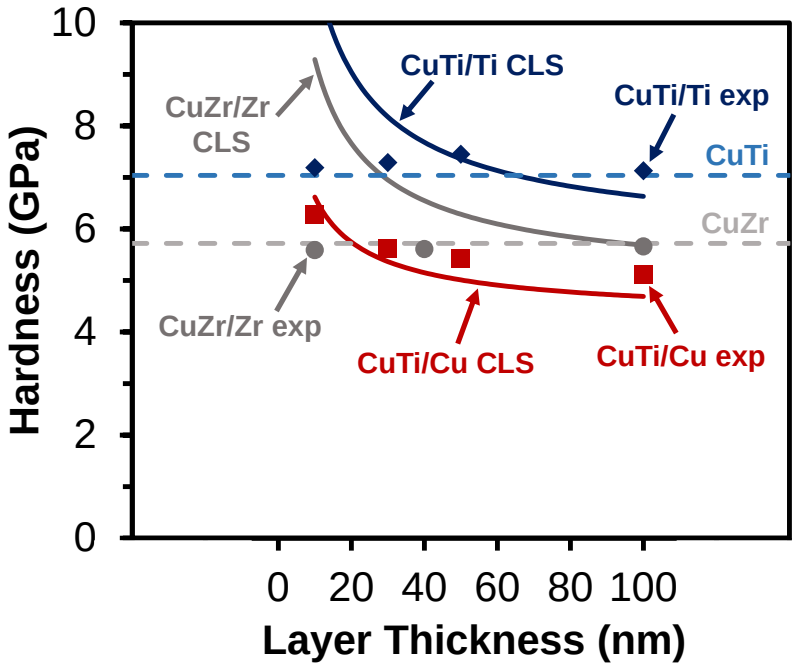

Figure 18. Comparison of the predictions of the confined layer slip (labeled as CLS) model with the experimental data (labeled as exp). Dashed lines indicate the hardness of the monolithic metallic glasses.

For CuTi/Ti and CuZr/Zr, prediction of the CLS model can be determined similarly. For CuTi, we keep the parameters governing the interface behavior the same, and adopt the remaining parameters from the previous work on Mg/Ti nanolayers [77]; b_{Ti} = 0.29 nm, ν = 0.32, φ = 60°, α = 0.45, f = 1.1 J/m^2, and L = 9 nm. CuZr/Zr can be modeled similarly, where b_{Zr} = 0.32 nm, ν = 0.34, φ = 60°, and

we keep α, f, and L the same as those of CuTi/Ti. Figure 18 shows that the predicted strengths of Ti and Zr confined in a layered geometry are higher than that of Cu.

More importantly, the confined layer slip in the crystalline layer, Ti (or Zr), requires a higher stress than the flow stress of monolithic CuTi (or CuZr). This result suggests that, during indentation of CuTi/Ti and CuZr/Zr, metallic glass layers deform before the crystalline layers. Then the strength of the composite and any associated size effect are expected to be dominated by the response of the metallic glass. As the metallic glass layers are of amorphous nature, it is not possible to apply the CLS model. Nevertheless, the results of layer thickness-independent hardness can be interpreted qualitatively. First of all, metallic glasses do not show a strong size effect when compared to the smaller-is-stronger behavior observed in crystalline materials. Compression studies on Pd-based bulk metallic glasses showed that the micropillar specimens with diameters in the range 2 – 20 μm are only ~10% stronger than their bulk counterparts [75]. A similar behavior is observed in confined geometries; a Zr-based/Pd-based amorphous/amorphous nanolayered film was reported to have a hardness of only 15% higher than those of its constituents [76]. These variations are much smaller when compared to crystalline metals; as an example, nanolayered Cu/Nb's strength can reach three times that of nanocrystalline Cu [30]. Therefore, the size-independent behavior of the metallic glasses can explain the virtually constant hardness of CuTi/Ti.

In addition to analyses by using the CLS model, the results can also be interpreted by the deformation behavior of HCP crystals. During the nanoindentation of CuTi/Ti and CuZr/Zr, basal planes are mostly perpendicular to the loading and the operation of the basal and prismatic slip is limited. The result is the operation of the prismatic slip planes. Cantilever bending measurements on single crystal Zr has shown that the critical resolved shear stress (CRSS) in the pyramidal planes can be more than two times higher than those of basal and prismatic planes [84].

Therefore, a geometric strengthening is expected in Zr layers, which will force the metallic glass layers to deformation. Ti also has a high CRSS for the pyramidal slip [85], and this can explain the high strength of CuTi/Ti layers when compared to the relatively low hardness of our nanocrystalline Ti that lacks texture. Such anomalous geometric strengthening has previously been observed in Mg/Nb HCP/BCC nanolayers with strongly textured Mg layers [39].

3.5. CONCLUSION

We investigated the structure-property relationships of two amorphous/HCP crystalline nanolayered systems, CuTi/Ti and CuZr/Zr. As opposed most C/C and A/C nanolayers reported to exhibit strengthening with decreasing layer thickness in the literature, amorphous/HCP nanolayers maintained virtually the same hardness for layer thicknesses in the range 10-100 nm. By using the confined layer slip model, we estimated that the crystalline layers, Ti and Zr, have higher effective flow strengths than those of the corresponding metallic glasses, CuTi, and CuZr. This prediction suggests that the strength and size effects of CuZr/Zr and CuTi/Ti nanocomposites are mostly governed by the response of the metallic glass constituent, in agreement with our experimental findings. We also explored a nanolayered amorphous/FCC crystalline composite of CuTi/Cu as a third model system and demonstrated the commonly observed strengthening with decreasing layer thickness, which can also be quantitatively explained by the confined layer slip model.

The layer thickness-independent strength observed for amorphous/HCP crystalline nanolayers gives insight into the mechanical behavior of metallic glasses and crystalline metals at the nanoscale and provides a convenient model system for the future studies about the effects of layer thickness on other mechanical properties such as ductility and fracture toughness.

CHAPTER 4

4. NANOSCRATCH BEHAVIOR OF METALLIC GLASS/CRYSTALLINE NANOLAYERED COMPOSITES

This chapter is reproduced with permission from Mohammad Abboud, Amir Motallebzadeh, Nisha Verma, and Sezer Özerinç, "Nanoscratch behavior of metallic glass/crystalline nanolayered composites", JOM, 2018 [60].

4.1. INTRODUCTION

One of the successful model systems that eliminate the need for a compromise between hardness and ductility has been the CuZr/Zr system formed by alternating layers of CuZr MG and nanocrystalline pure Zr [11]. Due to the similar mechanical properties of these two phases, the crystalline layer is not squeezed in between the MG layers upon loading, as opposed to what is observed in CuZr/Cu system [86]. Crystalline and amorphous layers co-deform upon loading, improving ductility; and the strength is close to that of the monolithic MG.

Although the high strength and hardness combined with large ductility makes CuZr/Zr a promising model system for wear resistant coating applications, there has been no study to date to investigate the wear behavior of this nanocomposite. In fact, there has been no study in the literature regarding the wear behavior of MG/crystalline nanolaminates apart from the wide literature that focuses on the ultra-hard superlattice coatings of metal nitrides and their composites [87].

Nanolayered metallic glass/crystalline composites provide an effective structure for improving the ductility of metallic glasses while maintaining their outstanding strength. Combination of high strength and ductility make these nanocomposites promising materials as wear resistant coatings.

In this work, we experimentally investigated the mechanical properties and nanoscratch behavior of CuZr/Zr metallic glass/crystalline nanolayers. The scratch resistance was highest for the monolithic CuZr, and diminished with decreasing layer thickness for nanolayered coatings, although hardness and elastic modulus were independent of layer thickness.

The nanocomposite with a layer thickness of 10 nm did not show any sign of failure in spite of compressive strain exceeding 80%. Low shear strength of the CuZr-Zr interface and strain hardening of Zr layers can explain the layer-thickness dependent scratch resistance and outstanding damage tolerance observed. Layered metallic glass/crystalline nanocomposites combine high hardness and resistance to fracture, providing a new design space for the development of effective wear resistant coatings.

Nanolayers with layer thicknesses in the range 10-100 nm were considered, which corresponds to the regime promoting the codeformation of the MG and crystalline layers for improved ductility [9,10]. We employed standard microstructural characterization techniques together with nanoindentation for mechanical property determination. Nanoscratch technique was utilized as a practical and repeatable approach for comparing the wear behavior of the coatings [57]. Analyses of CuZr/Zr for a range of layer thicknesses provided insight to the deformation morphology of these composites under severe strain conditions.

4.2. EXPERIMENTAL DETAILS

Table I shows a list of samples prepared for this study and their naming convention. CuZr is a monolithic MG thin film with an atomic composition of $Cu_{45}Zr_{55}$, as verified by energy dispersive X-Ray spectroscopy (EDS). CuZr/Zr samples are nanolayered films with alternating layers of $Cu_{45}Zr_{55}$ MG and pure nanocrystalline Zr. For these nanolayered samples, CuZr and Zr layers are of equal thickness. We prepared three different nanolayers with layer thicknesses of 10, 40, and 100 nm. The seed layers were CuZr in all nanolayered films. The total thickness of all of the coatings was 1 μm.

Table 4. List of the samples prepared for this study.

Sample Name	Composition	Layer Thickness
Zr	nanocrystalline Zr	1 μm monolithic
CuZr	$Cu_{45}Zr_{55}$	1 μm monolithic
CuZr/Zr-X	alternating layers of $Cu_{45}Zr_{55}$ and pure Zr	X = 10, 40, 100 nm
SS	316L stainless steel	bulk

We deposited the films on 316 stainless steel (SS) plates of 1 cm × 1 cm size and 0.5 mm thickness (McMaster-Carr, IL, USA). SS substrates were wet ground with 2000 grit paper, and further polished using 250 nm diamond polish. After polishing, an atomic force microscope scan over a 20 μm × 20 μm area indicated an average roughness of 2 nm.

In addition, a 40 nm thick CuZr film was deposited on transmission electron microscopy (TEM) grids containing 18 nm-thick freestanding SiO_2 windows (Ted Pella, CA, USA) for the quick verification of the amorphous structure. All the results presented are for the films on SS substrates unless otherwise indicated.

A VAKSİS magnetron sputterer (Turkey) equipped with two guns deposited all the samples. The base pressure of the chamber was about 1×10^{-7} Torr and the Ar pressure was 2.2×10^{-3} Torr during deposition. Sputtering targets were pure Cu (99.99% purity) and pure Zr (99.99% purity) disks of 2" diameter (Kurt J. Lesker, PA, USA). A ZYGO 7200 optical profilometer (CT, USA) measured the thickness of the deposited films and verified that the variation in film thickness is less than 5% over the samples.

An Ultima IV diffractometer (Rigaku, Japan) characterized the films in $\theta - 2\theta$ configuration. A Quanta 400F (FEI Company, OR, USA) scanning electron microscope (SEM) performed surface imaging and EDS (Oxford Instruments, UK). A Nova 600 Nanolab (FEI Company, OR, USA) focused ion beam (FIB) prepared the TEM samples by lift-out technique. A JEM2100F field-emission scanning TEM (JEOL, Japan) imaged the samples at 200 keV. A Dimension Icon (Bruker, MA, USA) atomic force microscope (AFM) scanned the topography of selected scratches in tapping mode. Five 90 μm × 90 μm scans performed along the scratches provided a full picture of the damage morphology.

An Agilent G200 nanoindenter (CA, USA) measured the hardness of the films by using a Berkovich tip in continuous stiffness measurement mode [57]. 15 indentations were performed on each sample. Reported hardness and elastic modulus values represent the data at a depth around %15 of the film thickness where hardness vs. depth curve featured a plateau.

The same nanoindenter performed the nanoscratch tests in ramping load mode. A sphero-conical diamond tip with 5 μm radius and an included angle of 90° was used. A sphero-conical tip was preferred, as the tip radius of sharp geometries such as Berkovich quickly increases in sliding load conditions, adversely affecting the repeatability of the measurements. The normal force increased linearly from 0 mN to 500 mN over a total scratch length of 500 μm. The scratch speed was 40 μm/s, resulting in a loading rate of 40 mN/s and 1 mN/μm. A relatively high scratch speed was employed to minimize the effects of drift and to improve repeatability. Before each test, the scratch path was scanned with a very low load of 50 μN to compensate for any slope or irregularity on the surface. The penetration depth vs. scratch length profiles show the average of 10 scratches for each sample, separated by at least 75 μm, which is larger than seven times the diameter of the indenter tip. The residual depth vs. scratch length profiles are based on AFM scans of selected scratches.

The FEI Nova 600 Nanolab FIB milled the cross-sections of selected scratches at the point of 400 mN normal force. We deposited a platinum cap of 1 μm thickness before cross-section milling to obtain a clean cross section and to protect the coating surface from ion beam damage.

4.3. RESULTS AND DISCUSSION

4.3.1. MICROSTRUCTURE

Figure 19 shows cross-sectional bright field TEM images of the CuZr/Zr samples with different layer thicknesses. Zr layers are polycrystalline whereas CuZr layers are featureless due to the amorphous structure. The inset on the left shows a high-resolution image of the disordered atomic structure in the MG layers. Zr grains have a columnar structure, and the inset on the right shows the diffraction of an area containing multiple layers. Diffraction from (002) planes is pronounced and texture is evident from the preferential orientation of high-intensity regions. The vertical lines of high brightness in CuZr layers are due to the nonuniform FIB milling and redeposition caused by the crystalline layers. On the other hand, Ga^+ bombardment did not induce any obvious ion-induced damage as crystalline and amorphous layers maintained their structure.

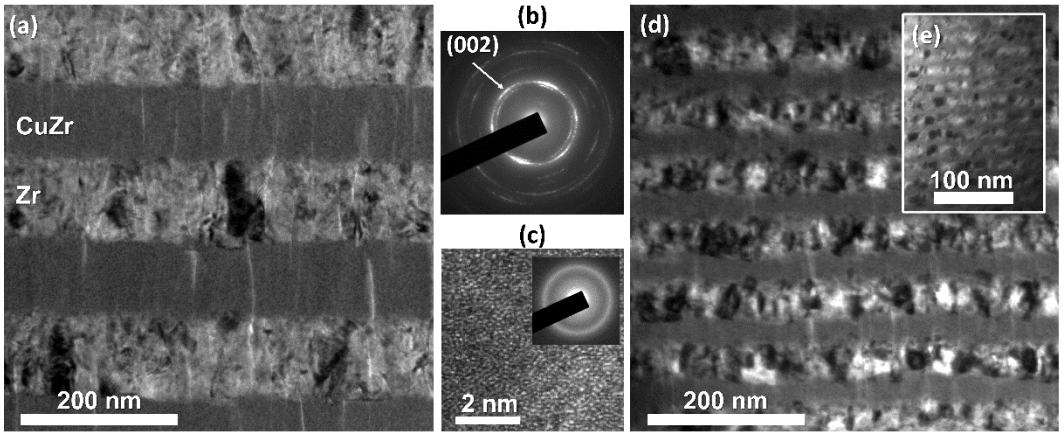

Figure 19. Cross-sectional bright field TEM image of (a) CuZr/Zr-100 nanolayers, (d) CuZr/Zr-40 nanolayers, and (e) CuZr/Zr-10 nanolayers. Figure (b) shows the diffraction pattern of the film from an area containing multiple layers, while figure (c) shows is a high-resolution TEM image of the amorphous layer with the diffraction pattern as an inset.

Figure 20 shows the XRD results of all samples deposited on SS. CuZr MG does not show any crystalline peak but a wide hump that is characteristic of fully amorphous materials. The diffraction pattern of the nanolayered film exhibits both the amorphous hump and the crystalline peaks as a result of the superposition of the reflections from the crystalline and the amorphous layers. (002) peaks are pronounced in Zr layers, in agreement with TEM results, indicating that basal planes are mostly aligned with the layer interfaces. This texture is similar to that observed previously in alternating layers of crystalline Cu/Zr multilayers [12]. The (002) intensity and associated texture become stronger with increasing layer thickness, another feature of confined Zr layers previously reported [40]. Glancing angle XRD measurements (not shown here) indicated a decrease in (101) peak intensity with increasing layer thickness, further confirming this variation in texture. Inset of figure 20 shows the grain size of Zr layers calculated from Scherrer equation based on (002) peaks. Grain size monotonically decreases with decreasing layer thickness, a dependence commonly encountered in nanolayers prepared by physical vapor deposition [40].

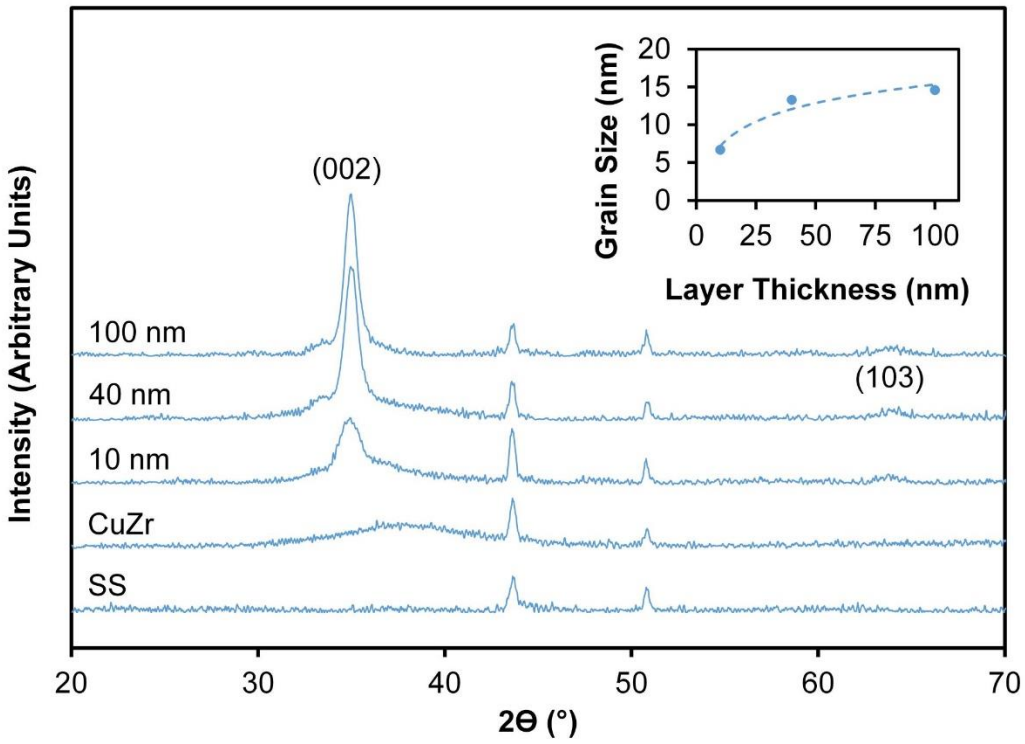

Figure 20. XRD patterns of CuZr MG, CuZr/Zr nanolayers (labeled with their respective layer thickness), and the uncoated SS substrate. Inset shows the grain size of Zr layers as a function of layer thickness.

4.3.2. MECHANICAL PROPERTIES

Figure 21 summarizes the hardness results for samples deposited on SS substrates. CuZr MG has a hardness of 5.72 ± 0.09 GPa, which is within the range of values reported for CuZr thin films in the literature [64,65]. Pure nanocrystalline Zr has a hardness of 7.03 ± 0.25 GPa, higher than the metallic glass. Hardness values of CuZr/Zr with 100, 40 and 10 nm layers are 5.66 ± 0.2 GPa, 5.61 ± 0.12 GPa, and 5.59 ± 0.1 GPa, respectively. Hardness values of CuZr/Zr nanolayers do not change considerably with layer thickness and are very close to that of monolithic CuZr. The figure inset shows the elastic modulus results. Similar to the trends in hardness, modulus does not depend strongly on layer thickness, and modulus of layered samples is very close to that of CuZr.

The hardness of our nanocrystalline Zr is 0.5 – 1 GPa higher than the values reported for nanocrystalline Zr with random texture [88], which can be interpreted by considering the effect of texture on the mechanical response. When Zr basal planes are perpendicular to the loading direction, which is the case for our measurements, basal slip and prismatic slip do not play a major role and pyramidal slip dominates the plasticity [40]. Critical resolved shear stress in single crystal Zr over pyramidal slip planes can exceed 500 MPa, more than twice that of the basal and prismatic planes, as measured by microcantilever bending experiments [84]. This strong anisotropy increases the resistance to plastic deformation when the texture and loading orientations favor pyramidal slip and can explain the high hardness measured for Zr. Micropillar compression experiments on (002) textured nanocrystalline Zr further support this argument [11]; the measured yield strength of ~2.6 GPa indicates a hardness of ~7.8 GPa, assuming a Tabor factor of 3 [63].

Most previous studies on nanolayered crystalline/crystalline and MG/crystalline composites reported an increase in strength with decreasing layer thickness [12,33,36].

Figure 21 shows an example of this trend for CuZr/Cu nanolayers, the composite hardness increases as layer thickness decreases, eventually reaching to that of monolithic CuZr at a layer thickness around 10 nm [12]. Our results for CuZr/Zr nanolayers do not show such dependency on layer thickness (see Figure 21).

Layer thickness-independent strength of CuZr/Zr can be interpreted by considering the relative strengths of the constituent layers. Since plastic deformation starts in the softer layers and continues until dislocation activity or shear transformations are induced in the harder layer, the softer layers tend to govern any size-dependent behavior. For MG/crystalline composites, an example is CuZr/Cu, where the confinement of Cu into layers both decrease the grain size and increase the density of interfaces acting as a barrier to dislocation motion. Associated hardening of the Cu layer with decreasing layer thickness is directly reflected in the hardness of the composite [12]. Among the crystalline/crystalline nanolayers, by far the most widely studied system is Cu/Nb, and its size dependency can also be explained by modeling the confined layer slip in Cu layers only [36].

In this work, as opposed to most studies in the literature, MG is the softer layer; therefore, any layer thickness dependence of the composite would depend on that of the MG layers. Although there is a limited number of studies on the size effects of MG/MG nanolayers when compared to other nanolayered composites, the results suggest that MG layers do not exhibit a strong size dependence in layered form. A micropillar compression and nanoindentation study on ZrCuTi/PdCuSi MG/MG nanolayers have shown that the strength of the MG in layered form is only about 15% higher than the monolithic counterparts [77], as opposed to a three-fold hardening observed in the strength of Cu-Nb when compared to monolithic Cu [30]. While these findings provide possible explanations for the size-independent strength in CuZr/Zr nanolaminates, there is a need for further investigation of this phenomenon by exploring other systems with hard crystalline layers. Our preliminary results suggest that such size-independence also exists in other MG/crystalline composite systems.

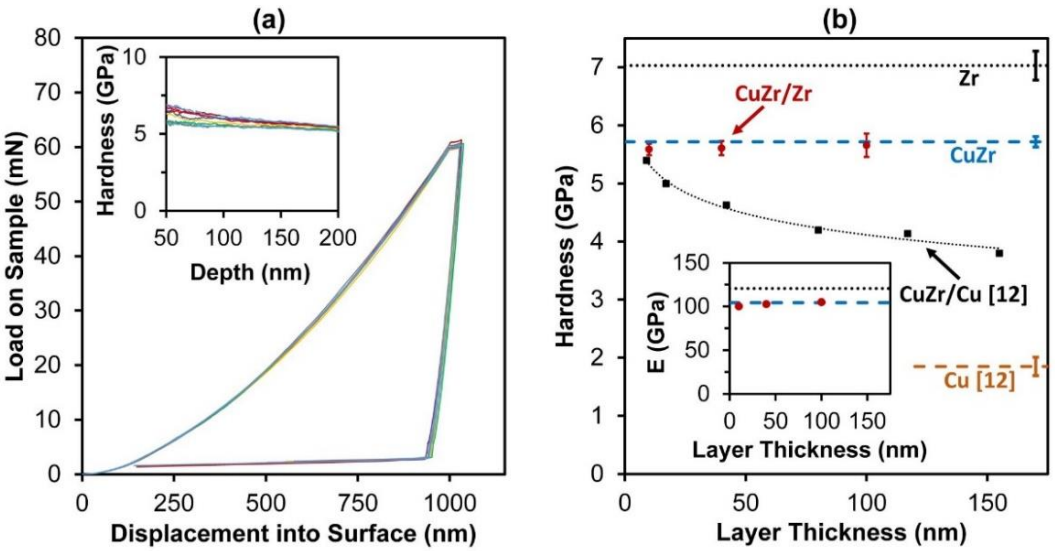

Figure 21. (a) Load-displacement curves of 10 nanoindentation tests on CuZr/Zr-100. Inset shows the variation of hardness with indentation depth. (b) Hardness of nanocrystalline Zr, CuZr MG, and CuZr/Zr nanolayers. CuZr/Cu and Cu hardness values [12] are shown for comparison. The inset shows elastic modulus (E) values of Zr, CuZr and CuZr/Zr using the same marker and line style convention as that of the main plot. The standard deviation of E is in the range 1-2 GPa for all samples respectively.

4.3.3. NANOSCRATCH BEHAVIOR

Figure 22 summarizes the results of nanoscratch testing. Figure 22a shows an example of a series of scratches on CuZr/Zr-40. Figure 22b is the corresponding penetration depth vs. scratch distance data, as measured by the nanoindenter during the scratch, demonstrating the repeatability of the measurements. Figure 22c summarizes the penetration depth profiles for all samples, where positive values indicate the displacement into the sample. The profiles represent the average of 10 scratch experiments for each sample. The inset on the bottom left shows the post-scratch residual depth profiles obtained by a series of AFM scans along selected scratches.

Before a complete discussion of the results, the contribution of the coatings to the scratch response needs to be clarified. The penetration of the indenter reaching 3 to 5 times the thickness of the coatings (Figure 22c) indicates severe substrate deformation. Nevertheless, the coatings remain intact throughout the scratches and keep deforming under the indenter, as discussed in greater detail later in this section. Therefore, the scratch response of the coatings is reflected in the results for the complete range of the scratches, which provide insight into their deformation behavior under severe strain, as discussed below.

The CuZr monolithic film demonstrates the smallest penetration depth and residual depth; therefore, has the highest scratch resistance among the coatings. The second most resistant coating is CuZr/Zr-100, and scratch resistance of the nanolayers diminish with decreasing layer thickness. Figure 22c also shows the scratch performance of uncoated SS for comparison, demonstrating that all coatings provide substantial wear resistance from a practical point of view. Both the penetration depth and residual depth increases monotonically with increasing load and scratch distance for all coatings. There is no sign of a critical point of abrupt depth change indicative of coating failure.

Detailed SEM imaging along the scratches also verified that coatings do not exhibit any major chipping or spallation. SEM images of scratch tracks of CuZr and CuZr/Zr-40 in Figure 23a and b demonstrate the integrity of the coatings at a load of ~400 mN.

Residual depth data in Figure 22c shows somewhat irregular variations in the scratch profile. The scratch tracks imaged by SEM do not exhibit a substantial amount of debris, and the deformation morphology of the coating is relatively smooth suggesting that these irregularities are not caused by the coating itself. On the other hand, the large grain size of the SS (~20 μm) and associated heterogeneity in the plastic response might be causing these variations in the depth profile. The periodicity of these irregularities is comparable to the SS grain size and at least an order of magnitude larger than the film thickness, which is also indicative of the role of the substrate. Nevertheless, this heterogeneity does not completely override the scratch response of the coatings, and unique resistance of each coating to scratch is clearly distinguishable.

Figure 22d and e show the residual transverse-profiles of selected scratch tracks at the locations of 250 mN and 400 mN loading, respectively. The coatings with larger penetration and residual depth show more pronounced pile-up for both regions considered. At a loading of 400 mN, a pile-up in for CuZr/Zr-10 reaches a height of ~2 μm – twice the film thickness; indicating that the plastic deformation of the substrate contributes to pile-up.

Figure 23 compares the deformation morphology of the coatings. Figure 23a and b show SEM images of scratch tracks for CuZr and CuZr/Zr-10 at a load of ~400 mN. Neither of the coatings shows a sign of gross failure; however, CuZr shows indications of local fracture near the center of the track where the strain is the highest. On the other hand, CuZr/Zr-10 demonstrates smooth lines of deformation along the scratch, without any sign of fracture, in spite of the larger strain and bigger pile-up when compared to CuZr for the given loading. Other nanolayered CuZr/Zr coatings demonstrated similar morphology, there was no visible fracture throughout the scratches.

There are regions with substantial pile-up near the edges of the scratch track, corresponding to irregularities in the residual depth profiles. The damage morphology in these regions gives insight into the effect of layer thickness on the plastic response. Figure 23c and d compare the SEM images of CuZr/Zr-10 and CuZr/Zr-100 around selected regions of the severe pile-up. Both images correspond to a loading of ~400 mN. Figure 23c shows that CuZr/Zr-10 has relatively small shear band spacing indicative of higher ductility when compared to CuZr/Zr-100. The pile-up region in the CuZr/Zr-100 features larger shear band spacing, and the coating fractures at multiple locations in a brittle fashion, with fracture surfaces being perpendicular to shear bands.

Layer-thickness dependent scratch resistance observed in this study for coatings of very similar hardness and elastic modulus is an interesting observation and gives insight to the mechanical behavior of nanolayered composites at the small scale. Since the elastic modulus of all coatings are virtually the same within experimental uncertainties, any difference in the penetration depth profiles shown in Figure 22c comes from the plastic part of the response, as verified by the residual depth profiles (inset of Figure 22c). The penetration profiles of all coatings are very close to each other up to a scratch distance of about 150 μm, and associated residual profiles indicate a similar trend. This is not surprising for coatings of similar hardness and elastic modulus. However, beyond 150 μm, the scratch resistance diminishes with decreasing layer thickness, or in other words, with an increasing number of crystalline-amorphous interfaces.

Since the possibility of a major change in the strength of the individual layers with layer thickness is ruled out by the invariant hardness and modulus (see figure 21), we focus on the role of the interfaces. Recent measurements on micropillars of tilted nanolayers revealed that the interface strength in between CuZr and Zr is lower than the intrinsic shear strength of the constituent layers [89]. This relatively weak interface might not play a major role when loading direction is normal to the interface, but it would ease plastic deformation when the strain is high and/or when the loading condition geometrically favors sliding along the interface.

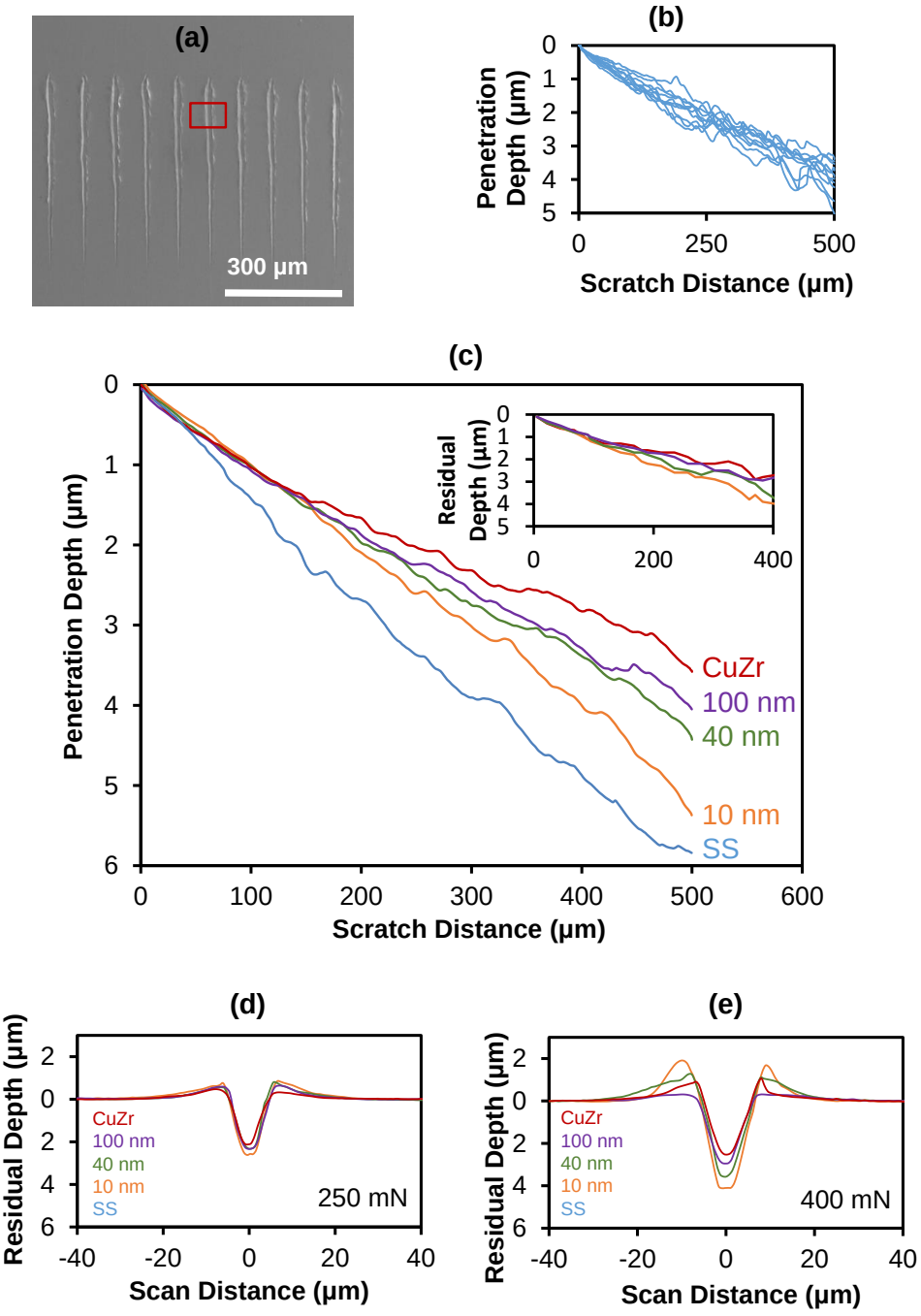

Figure 22. (a) SEM image of 10 scratches on CuZr/Zr-40. The red rectangle represents the region of FIB cross-sectioning (see Figure 24). (b) 10 penetration depth profiles for CuZr/Zr-40 measured during scratch loading, demonstrating the repeatability of the measurements. (c) Penetration depth profiles for each sample,

measured during scratch loading. Each curve represents the average of 10 scratches for the associated sample. The inset at the top right shows the residual scratch depths, as measured by AFM at ~20 μm intervals along selected scratches. The sample ordering of the residual depths is the same as that of the penetration depth. (d, e) Scratch track profiles measured by AFM on selected scratches at locations of 250 mN and 400 mN loading, respectively.

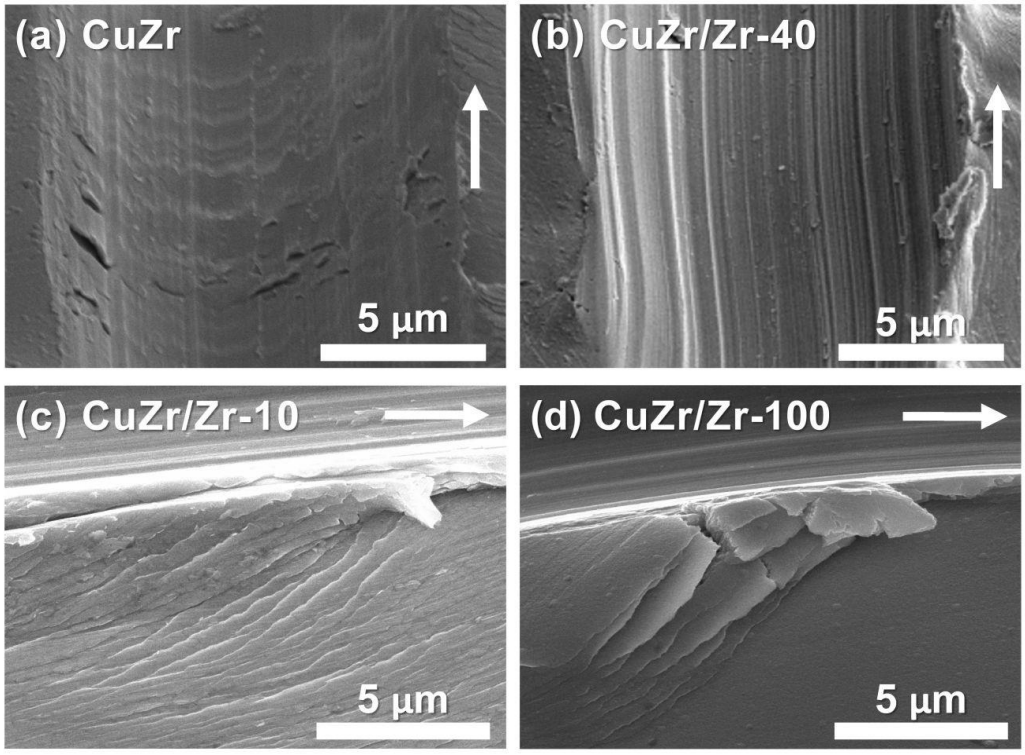

Figure 23. SEM images showing the scratch tracks (a) CuZr, and (b) CuZr/Zr-10. The images have a tilt of 52°. SEM images of pile-up behavior near the edge of the scratch track for (c) CuZr/Zr-10, and (d) CuZr/Zr-100. The arrows indicate the scratch direction. All images are taken at a location of ~400 mN loading of selected scratches.

Our hardness results do not change with the layer thickness (interface density), as stress is predominantly normal to the layers in nanoindentation, and the average strain of 8% [74] would not geometrically require a significant amount of sliding in between layers. Similarly, at the initial part of a scratch, there is a relatively small strain on the coating, and as a result, there is virtually no difference between the penetration depths measured. However, as the scratch proceeds, compressive strain experienced by the coatings increases. Compressive engineering strain perpendicular to the substrate can be estimated by comparing the thickness of the coatings before and after the scratch test, using cross-sectional SEM measurements (see Figure 24 for an example). This approach indicates a compressive strain exceeding 60% at the center of the wear track at a load of 400 mN for all samples. As the strain calculation is based on the thickness of the coatings before and after scratch testing, resulting in an engineering strain perpendicular to the substrate.

Furthermore, we also observed some variations in the deformed layer thicknesses on the cross-sections of the scratch tracks. Both the excessive pile-up induced by the high strain and the nonuniform compressive strain in the layers promote interfacial sliding. Under these conditions, the presence of a larger number of interfaces eases the plastic deformation and decreases the resistance to scratch penetration. The interface dominated wear behavior explains both the observation that the highest scratch resistance occurs for the CuZr with no interfaces, and that the scratch resistance monotonically decreases with increasing number of interfaces. A second parameter that might contribute to the layer-thickness dependent wear resistance is strain hardening. As the grain size and/or layer thickness decreases below about 100 nm in a crystalline metal, grain boundary sliding starts to dominate over dislocation-mediated plasticity and strain hardening associated with dislocation interactions diminishes [90]. As dislocation activity decreases not abruptly but gradually with decreasing layer thickness in the range 100 – 10 nm, CuZr/Zr-100 is expected to possess higher strain hardening than CuZr/Zr-10. Then the higher strain hardening in the CuZr/Zr-100 can explain the increased wear resistance in regions of a higher strain.

In light of the damage morphologies and scratch resistance performance, a compromise is evident between scratch resistance and fracture resistance. Monolithic CuZr shows superior performance in terms of resistance to plastic deformation. On the contrary, CuZr/Zr-10 with inferior scratch resistance does not show any sign of fracture even in the pile-up regions, in spite of experiencing compressive strain levels exceeding 80% at the center of the track (see inset of Figure 24b). This nanolayered structure that combines high hardness and fracture resistance is especially promising for protective coating applications on compliant substrates such as magnesium and aluminum components widely used in automotive industry, and/or applications of impact wear resistance where substrate deformation is severe. Furthermore, our preliminary studies of the application of the same coatings on oxidized silicon substrates resulted in almost identical microstructure and mechanical properties to that of the coatings on SS, suggesting that the coatings can be applied to a wide range of substrates with different microstructure and mechanical properties.

The layered coatings also provide excellent adhesion and conformity when the substrate deformation is extreme. Figure 24 demonstrates an example of this for the CuZr/Zr-40 where a FIB cross-section was prepared intentionally at a region of somewhat irregular and excessive pile-up mostly induced by the substrate. The close-up view of the pile-up region shows no signs of delamination or buckling and the coating remains intact. The previous TEM analysis of the interface between a sputtered Zr-based MG and SS indicated that an interfacial layer forms between the coating and substrate resulting from interatomic mixing [77]. This observation can explain the good adhesion and conformity of the coating to the substrate. Ultra-high plasticity of MG thin films under compressive loading has also been observed in other Zr-based MGs [91], and the lack of fracture in our films for strains exceeding 80% provides additional evidence for the excellent damage tolerance of MGs in confined geometries. The continuity of the coating upon severe bending and strain is desirable for applications that require combined wear and corrosion resistant.

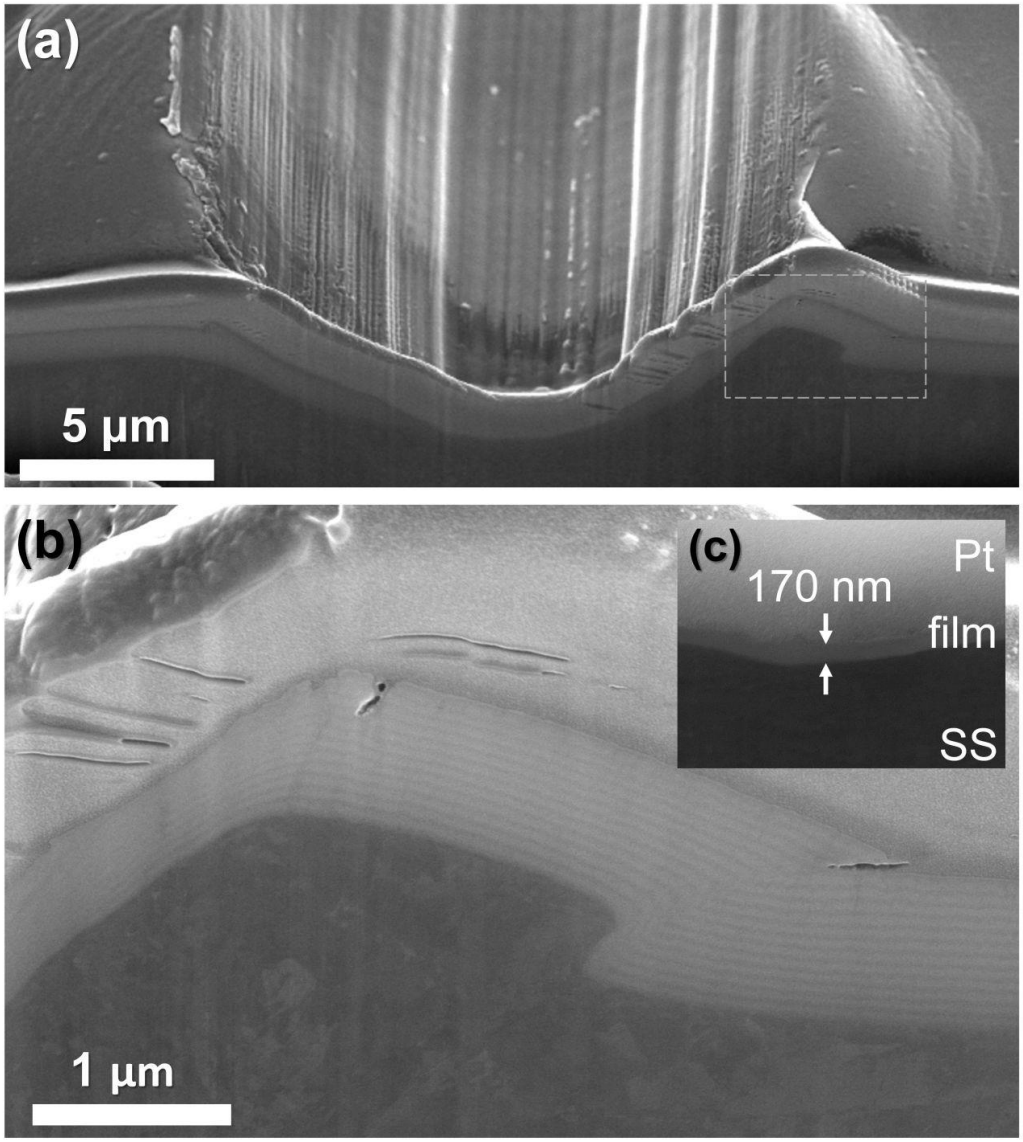

Figure 24. (a) SEM cross-sectional view of CuZr/Zr-40 and (b) a close-up view of the pile-up region in (a) marked with the dashed rectangle. (c) SEM cross-sectional view of high strain experienced by CuZr/Zr-10 in the center of the scratch track.

4.4. CONCLUSION

We investigated the mechanical properties and nanoscratch behavior of monolithic CuZr metallic glass and CuZr/Zr metallic glass/crystalline nanolayered coatings deposited on stainless steel. Hardness and elastic modulus of CuZr/Zr coatings do not depend on layer thickness and are virtually the same as that of monolithic CuZr. We attribute this size-independent strength to the unique combination of a softer metallic glass with a harder nanocrystalline metal, where the metallic glass layer does not exhibit a strong size effect.

Nanoscratch experiments showed that CuZr is the most scratch resistant coating and scratch resistance decreases with decreasing layer thickness and increasing interface density. Different scratch performance observed for coatings of similar hardness and elastic modulus gives insight to the deformation behavior of metallic glass nanocomposites. We explain the layer thickness-dependent scratch resistance by the increase in interfacial sliding with decreasing layer thickness.

At the expense of relatively lower wear resistance, nanolayered CuZr/Zr coatings demonstrated outstanding adhesion and conformity to the substrate for compressive strains exceeding 80% without any sign of major failure. While this finding demonstrates the effectiveness of metallic glass/crystalline composites in improving the ductility of metallic glasses, it also opens a new design space for the development of wear resistant coatings for compliant substrates and/or impact wear conditions with severe substrate deformation. For these applications, exploring MG-based nanolaminates with higher hardness would be necessary, as the hardness of the CuZr/Zr coatings cannot compete with the commercial hard coatings. Refractory element-based MGs and nanostructured alloys are promising routes towards this objective. In addition, future studies focusing on nanolayers with intentional mechanical property mismatch and amorphous/amorphous nanolayers will provide further assessment of the great potential of metallic glass thin films for wear applications.

5. CONCLUSIONS AND FUTURE WORK

In this work, the nanomechanical properties of nanocomposite metallic glasses have been investigated using nanomechanical characterization techniques such as the nanoindentation and the nanoscratch techniques. Additionally, theoretical calculations were done to further interpret the results.

Two amorphous/HCP crystalline nanolayered systems were investigated, CuTi/Ti and CuZr/Zr. These multilayered film has been proposed as an alternative to the traditional amorphous – crystalline system with Cu as the crystalline intermediate layer. In contrary to the traditional system, CuTi/Ti and CuZr/Zr did not lose its hardness as the individual layer thickness was increased. This was mainly due to the fact that Ti and Zr have HCP crystal structures and that of Cu is FCC. The deformation was governed by the softer amorphous layer, but not by the crystalline ones as opposed to the cases in the literature. These results were interpreted in the light of the confined layer slip model calculations. Due to the fact that CLS model assumes that the crystalline layer deforms first, it helped predicting the behavior of CuTi-Cu, but failed to predict the ones that had HCP intermediate crystalline layers.

In addition to the aforementioned testing, amorphous CuZr – Crystalline Zr hardness wear resistance properties were investigated using nanoscratch tests. Results show a decrease in scratch resistance as the number of layers in the film increases. This is attributed to the resulting stress concentration at the interfaces between the layers. Further, the fact that thicker layers allow for more strain hardening might have contributed to the higher scratch resistance observed in thicker layers. Shear band size was observing to increase as layer thickness was increased. On the other hand, Pile-up was observed to be higher for coatings with thinner layers and more compressive strain. Damage tolerance was higher in the multilayered layers and decreased as layer thickness increased.

As a future work, the structural and mechanical properties of binary metallic glass alloys are being investigated. Combinatorial magnetron sputtering was used to characterize 14 different compositions of CuNb thin films in the range Cu80Nb20 – Cu30Nb70. In spite of their immiscibility in the solid state, Cu and Nb form an amorphous structure over a wide range of compositions as verified by XRD and TEM. Nanoindentation hardness monotonically varies from 7 to 9 GPa with the composition of the metallic glass. These high hardness values can be related to the previous findings of the low free energy of amorphous CuNb caused by nanoscale phase separation into Cu-rich and Nb-rich regions.

Hardness tests and micropillar compression tests have been employed to probe the mechanical properties of AlTb metallic glasses. Results show an increase in hardness and yield strength as samples were annealed and a gradual increase as annealing temperature was increased from 241°C to 263°C. Hardness increased from around 4 GPa to almost 6 GPa, while yield strength increased from around 0.75 GPa to almost 1.25 GPa. On the other hand, ductility decreased as annealing temperature was increased.

Furthermore, experiments that enable the calculation of the fracture toughness of hard thin films, such as microcantilever beam bending tests and fracture toughness nanoindentation tests, are currently being done.

Overall, layered metallic glass/crystalline nanocomposites combine high hardness and resistance to fracture, providing a new design space for the development of effective wear resistant coatings.

REFERENCES

[1] W.H. Wang, C. Dong, C.H. Shek, Bulk metallic glasses, Mater. Sci. Eng. R Rep. 44 (2004) 45–89. doi:10.1016/j.mser.2004.03.001.

[2] A. Inoue, A. Takeuchi, Recent development and application products of bulk glassy alloys, Acta Mater. 59 (2011) 2243–2267. doi:10.1016/j.actamat.2010.11.027.

[3] M. Telford, The case for bulk metallic glass, Mater. Today. 7 (2004) 36–43. doi:10.1016/S1369-7021(04)00124-5.

[4] J.P. Chu, J.S.C. Jang, J.C. Huang, H.S. Chou, Y. Yang, J.C. Ye, Y.C. Wang, J.W. Lee, F.X. Liu, P.K. Liaw, Y.C. Chen, C.M. Lee, C.L. Li, C. Rullyani, Thin film metallic glasses: Unique properties and potential applications, Thin Solid Films. 520 (2012) 5097–5122. doi:10.1016/j.tsf.2012.03.092.

[5] J. Schroers, Q. Pham, A. Desai, Thermoplastic Forming of Bulk Metallic Glass amp;mdash; A Technology for MEMS and Microstructure Fabrication, J. Microelectromechanical Syst. 16 (2007) 240–247. doi:10.1109/JMEMS.0007.892889.

[6] J.S. Langer, Shear-transformation-zone theory of deformation in metallic glasses, Scr. Mater. 54 (2006) 375–379. doi:10.1016/j.scriptamat.2005.10.005.

[7] T.C. Hufnagel, C.A. Schuh, M.L. Falk, Deformation of metallic glasses: Recent developments in theory, simulations, and experiments, Acta Mater. 109 (2016) 375–393. doi:10.1016/j.actamat.2016.01.049.

[8] D.C. Hofmann, J.-Y. Suh, A. Wiest, G. Duan, M.-L. Lind, M.D. Demetriou, W.L. Johnson, Designing metallic glass matrix composites with high toughness and tensile ductility, Nature. 451 (2008) 1085–1089. doi:10.1038/nature06598.

[9] Y. Wang, J. Li, A.V. Hamza, T.W. Barbee, Ductile crystalline–amorphous nanolaminates, Proc. Natl. Acad. Sci. 104 (2007) 11155–11160. doi:10.1073/pnas.0702344104.

[10] W. Guo, E. Jägle, J. Yao, V. Maier, S. Korte-Kerzel, J.M. Schneider, D. Raabe, Intrinsic and extrinsic size effects in the deformation of amorphous CuZr/nanocrystalline Cu nanolaminates, Acta Mater. 80 (2014) 94–106. doi:10.1016/j.actamat.2014.07.027.

[11] M.C. Liu, J.C. Huang, H.S. Chou, Y.H. Lai, C.J. Lee, T.G. Nieh, A nanoscaled underlayer confinement approach for achieving extraordinarily plastic amorphous thin film, Scr. Mater. 61 (2009) 840–843. doi:10.1016/j.scriptamat.2009.07.010.

[12] J.Y. Zhang, Y. Liu, J. Chen, Y. Chen, G. Liu, X. Zhang, J. Sun, Mechanical properties of crystalline Cu/Zr and crystal–amorphous Cu/Cu–Zr multilayers, Mater. Sci. Eng. A. 552 (2012) 392–398. doi:10.1016/j.msea.2012.05.056.

[13] S.R. Agnew, B.R. Elliott, C.J. Youngdahl, K.J. Hemker, J.R. Weertman, Microstructure and mechanical behavior of nanocrystalline metals, Mater. Sci. Eng. A. 285 (2000) 391–396.

[14] C. Schuh, T. Hufnagel, U. Ramamurty, Mechanical behavior of amorphous alloys, Acta Mater. 55 (2007) 4067–4109. doi:10.1016/j.actamat.2007.01.052.

[15] W.K. Jun, R.H. Willens, P. Duwez, Non-crystalline Structure in Solidified Gold–Silicon Alloys, Nature. 187 (1960) 869–870. doi:10.1038/187869b0.

[16] A. Inoue, T. Zhang, T. Masumoto, Zr–Al–Ni Amorphous Alloys with High Glass Transition Temperature and Significant Supercooled Liquid Region, Mater. Trans. JIM. 31 (1990) 177–183. doi:10.2320/matertrans1989.31.177.

[17] W.L. Johnson, Bulk Glass-Forming Metallic Alloys: Science and Technology, MRS Bull. 24 (1999) 42–56. doi:10.1557/S0883769400053252.

[18] F.X. Liu, F.Q. Yang, Y.F. Gao, W.H. Jiang, Y.F. Guan, P.D. Rack, O. Sergic, P.K. Liaw, Micro-scratch study of a magnetron-sputtered Zr-based metallic-glass film, Surf. Coat. Technol. 203 (2009) 3480–3484. doi:10.1016/j.surfcoat.2009.05.017.

[19] C.W. Chu, J.S.C. Jang, S.M. Chiu, J.P. Chu, Study of the characteristics and corrosion behavior for the Zr-based metallic glass thin film fabricated by pulse magnetron sputtering process, Thin Solid Films. 517 (2009) 4930–4933. doi:10.1016/j.tsf.2009.03.049.

[20] C.T. Liu, L. Heatherly, J.A. Horton, D.S. Easton, C.A. Carmichael, J.L. Wright, J.H. Schneibel, M.H. Yoo, C.H. Chen, A. Inoue, Test environments and mechanical properties of Zr-base bulk amorphous alloys, Metall. Mater. Trans. A. 29 (1998) 1811–1820. doi:10.1007/s11661-998-0004-6.

[21] M.M. Trexler, N.N. Thadhani, Mechanical properties of bulk metallic glasses, Prog. Mater. Sci. 55 (2010) 759–839. doi:10.1016/j.pmatsci.2010.04.002.

[22] A.C. Lund, C.A. Schuh, The Mohr-Coulomb criterion from unit shear processes in metallic glass, Intermetallics. 12 (2004) 1159–1165. doi:10.1016/j.intermet.2004.07.001.

[23] P.E. Donovan, Compressive deformation of amorphous Pd40Ni40P20, Mater. Sci. Eng. 98 (1988) 487–490. doi:10.1016/0025-5416(88)90213-3.

[24] W.J. Wright, R.B. Schwarz, W.D. Nix, Localized heating during serrated plastic flow in bulk metallic glasses, Mater. Sci. Eng. A. 319–321 (2001) 229–232. doi:10.1016/S0921-5093(01)01066-8.

[25] P. Wesseling, P. Lowhahphandu, J.J. Lewandowski, Effects of superimposed pressure on flow and fracture of two bulk amorphous metals, Mater. Res. Soc. Symp. - Proc. 754 (2003) 275–279.

[26] Z.F. Zhang, J. Eckert, L. Schultz, Difference in compressive and tensile fracture mechanisms of Zr59Cu20Al10Ni8Ti3 bulk metallic glass, Acta Mater. 51 (2003) 1167–1179. doi:10.1016/S1359-6454(02)00521-9.

[27] F. Spaepen, A microscopic mechanism for steady state inhomogeneous flow in metallic glasses, Acta Metall. 25 (1977) 407–415. doi:10.1016/0001-6160(77)90232-2.

[28] A.S. Argon, Plastic deformation in metallic glasses, Acta Metall. 27 (1979) 47–58. doi:10.1016/0001-6160(79)90055-5.

[29] H. Jia, G. Wang, S. Chen, Y. Gao, W. Li, P.K. Liaw, Fatigue and fracture behavior of bulk metallic glasses and their composites, Prog. Mater. Sci. 98 (2018) 168–248. doi:10.1016/j.pmatsci.2018.07.002.

[30] N.A. Mara, D. Bhattacharyya, P. Dickerson, R.G. Hoagland, A. Misra, Deformability of ultrahigh strength 5nmCu⁄Nb nanolayered composites, Appl. Phys. Lett. 92 (2008) 231901. doi:10.1063/1.2938921.

[31] A. Misra, R.G. Hoagland, ‡ H.K., Thermal stability of self-supported nanolayered Cu/Nb films, Philos. Mag. 84 (2004) 1021–1028. doi:10.1080/14786430310001659480.

[32] M.J. Demkowicz, R.G. Hoagland, J.P. Hirth, Interface Structure and Radiation Damage Resistance in Cu-Nb Multilayer Nanocomposites, Phys. Rev. Lett. 100 (2008) 136102. doi:10.1103/PhysRevLett.100.136102.

[33] J. Wang, Q. Zhou, S. Shao, A. Misra, Strength and plasticity of nanolaminated materials, Mater. Res. Lett. 5 (2017) 1–19. doi:10.1080/21663831.2016.1225321.

[34] N. Li, J. Wang, A. Misra, J.Y. Huang, Direct observations of confined layer slip in Cu/Nb multilayers, Microsc. Microanal. Off. J. Microsc. Soc. Am. Microbeam Anal. Soc. Microsc. Soc. Can. 18 (2012) 1155–1162. doi:10.1017/S143192761200133X.

[35] M.A. Phillips, B.M. Clemens, W.D. Nix, A model for dislocation behavior during deformation of Al/Al3Sc (fcc/L12) metallic multilayers, Acta Mater. 51 (2003) 3157–3170. doi:10.1016/S1359-6454(03)00127-7.

[36] A. Misra, J.P. Hirth, R.G. Hoagland, Length-scale-dependent deformation mechanisms in incoherent metallic multilayered composites, Acta Mater. 53 (2005) 4817–4824. doi:10.1016/j.actamat.2005.06.025.

[37] M.C. Liu, X.H. Du, I.C. Lin, H.J. Pei, J.C. Huang, Superplastic-like deformation in metallic amorphous/crystalline nanolayered micropillars, Intermetallics. 30 (2012) 30–34. doi:10.1016/j.intermet.2012.03.037.

[38] Z. Fan, S. Xue, J. Wang, K.Y. Yu, H. Wang, X. Zhang, Unusual size dependent strengthening mechanisms of Cu/amorphous CuNb multilayers, Acta Mater. 120 (2016) 327–336. doi:10.1016/j.actamat.2016.08.064.

[39] B. Ham, X. Zhang, High strength Mg/Nb nanolayer composites, Mater. Sci. Eng. A. 528 (2011) 2028–2033. doi:10.1016/j.msea.2010.10.101.

[40] M. Callisti, T. Polcar, Combined size and texture-dependent deformation and strengthening mechanisms in Zr/Nb nano-multilayers, Acta Mater. 124 (2017) 247–260. doi:10.1016/j.actamat.2016.11.007.

[41] Q.M. Mehran, M.A. Fazal, A.R. Bushroa, S. Rubaiee, A Critical Review on Physical Vapor Deposition Coatings Applied on Different Engine

Components, Crit. Rev. Solid State Mater. Sci. 43 (2018) 158–175. doi:10.1080/10408436.2017.1320648.

[42] P.J. Kelly, R.D. Arnell, Magnetron sputtering: a review of recent developments and applications, Vacuum. 56 (2000) 159–172. doi:10.1016/S0042-207X(99)00189-X.

[43] M.A. Haque, M.T.A. Saif, A review of MEMS-based microscale and nanoscale tensile and bending testing, Exp. Mech. 43 (2003) 248–255. doi:10.1007/BF02410523.

[44] D.N. Allsopp, I.M. Hutchings, Micro-scale abrasion and scratch response of PVD coatings at elevated temperatures, Wear. 251 (2001) 1308–1314. doi:10.1016/S0043-1648(01)00755-4.

[45] S.J. Bull, Failure modes in scratch adhesion testing, Surf. Coat. Technol. 50 (1991) 25–32.

[46] W.C. Oliver, G.M. Pharr, An improved technique for determining hardness and elastic modulus using load and displacement sensing indentation experiments, J. Mater. Res. 7 (1992) 1564–1583. doi:10.1557/JMR.1992.1564.

[47] J.R. Cahoon, W.H. Broughton, A.R. Kutzak, The determination of yield strength from hardness measurements, Metall. Trans. 2 (1971) 1979–1983. doi:10.1007/BF02913433.

[48] T.Y. Tsui, J. Vlassak, W.D. Nix, Indentation plastic displacement field: Part II. The case of hard films on soft substrates, J. Mater. Res. 14 (1999) 2204–2209. doi:10.1557/JMR.1999.0296.

[49] ASTM Scratch Hardness of Materials Using a Diamond Stylus, 2017. https://compass.astm.org/download/G171.24869.pdf (accessed January 13, 2017).

[50] C. ASTM, ASTM Adhesion Strength and Mechanical Failure Modes of Ceramic Coatings by Quantitative Single Point Scratch Testing, n.d.

[51] B. Ingham, M.F. Toney, X-ray diffraction for characterizing metallic films, in: Met. Films Electron. Opt. Magn. Appl., Elsevier, 2014: pp. 3–38. doi:10.1533/9780857096296.1.3.

[52] J.I. LANGFORD, A.J.C. WILSON, Seherrer after Sixty Years: A Survey and Some New Results in the Determination of Crystallite Size, (n.d.) 12.

[53] K.C.A. Smith, C.W. Oatley, The scanning electron microscope and its fields of application, Br. J. Appl. Phys. 6 (1955) 391. doi:10.1088/0508-3443/6/11/304.

[54] C.A. Volkert, A.M. Minor, Focused Ion Beam Microscopy and Micromachining, MRS Bull. 32 (2007) 389–399. doi:10.1557/mrs2007.62.

[55] X. Li, B. Bhushan, A review of nanoindentation continuous stiffness measurement technique and its applications, Mater. Charact. 48 (2002) 11–36. doi:10.1016/S1044-5803(02)00192-4.

[56] M. Abboud, Sezer Özerinç, Size independent strength of amorphous – HCP crystalline metallic nanolayers, JMR. (2018).

[57] X. Li, B. Bhushan, A review of nanoindentation continuous stiffness measurement technique and its applications, Mater. Charact. 48 (2002) 11–36. doi:10.1016/S1044-5803(02)00192-4.

[58] S. Kabekkodu, ICDD 2016 Powder Diffraction File Inorganic and Organic Data Book, International Centre for Diffraction Data, PA, USA, 2016.

[59] S. Özerinç, K. Tai, N.Q. Vo, P. Bellon, R.S. Averback, W.P. King, Grain boundary doping strengthens nanocrystalline copper alloys, Scr. Mater. 67 (2012) 720–723. doi:10.1016/j.scriptamat.2012.06.031.

[60] M. Abboud, A. Motallebzadeh, N. Verma, S. Özerinç, Nanoscratch Behavior of Metallic Glass/Crystalline Nanolayered Composites, JOM. (2018). doi:10.1007/s11837-018-3270-9.

[61] S. Mao, S. Özerinç, W.P. King, R.S. Averback, S.J. Dillon, Effect of irradiation damage on the shear strength of Cu–Nb interfaces, Scr. Mater. 90–91 (2014) 29–32. doi:10.1016/j.scriptamat.2014.07.009.

[62] Z.C. Cordero, B.E. Knight, C.A. Schuh, Six decades of the Hall–Petch effect – a survey of grain-size strengthening studies on pure metals, Int. Mater. Rev. 61 (2016) 495–512. doi:10.1080/09506608.2016.1191808.

[63] D. Tabor, The Hardness of Metals, OUP Oxford, 2000.

[64] Z.T. Wang, K.Y. Zeng, Y. Li, The correlation between glass formation and hardness of the amorphous phase, Scr. Mater. 65 (2011) 747–750. doi:10.1016/j.scriptamat.2011.06.043.

[65] M. Apreutesei, P. Steyer, L. Joly-Pottuz, A. Billard, J. Qiao, S. Cardinal, F. Sanchette, J.M. Pelletier, C. Esnouf, Microstructural, thermal and mechanical behavior of co-sputtered binary Zr–Cu thin film metallic glasses, Thin Solid Films. 561 (2014) 53–59. doi:10.1016/j.tsf.2013.05.177.

[66] B. Gr[zcirc]eta, M. Stubiĉar, N. Cowlam, R. Trojko, Crystallization of Cu50Ti50 and Cu66Ti34 metallic glasses, Philos. Mag. A. 55 (1987) 227–236. doi:10.1080/01418618708209847.

[67] H.S. Chou, J.C. Huang, L.W. Chang, T.G. Nieh, Structural relaxation and nanoindentation response in Zr–Cu–Ti amorphous thin films, Appl. Phys. Lett. 93 (2008) 191901. doi:10.1063/1.2999592.

[68] A. Misra, M. Verdier, Y.C. Lu, H. Kung, T.E. Mitchell, M. Nastasi, J.D. Embury, Structure and mechanical properties of Cu-X (X = Nb,Cr,Ni) nanolayered composites, Scr. Mater. 39 (1998) 555–560. doi:10.1016/S1359-6462(98)00196-1.

[69] H. Huang, F. Spaepen, Tensile testing of free-standing Cu, Ag and Al thin films and Ag/Cu multilayers, Acta Mater. 48 (2000) 3261–3269. doi:10.1016/S1359-6454(00)00128-2.

[70] J. McKeown, A. Misra, H. Kung, R.G. Hoagland, M. Nastasi, Microstructures and strength of nanoscale Cu–Ag multilayers, Scr. Mater. 46 (2002) 593–598. doi:10.1016/S1359-6462(02)00036-2.

[71] J.Y. Zhang, X. Zhang, R.H. Wang, S.Y. Lei, P. Zhang, J.J. Niu, G. Liu, G.J. Zhang, J. Sun, Length-scale-dependent deformation and fracture behavior of Cu/X (X=Nb, Zr) multilayers: The constraining effects of the ductile phase on the brittle phase, Acta Mater. 59 (2011) 7368–7379. doi:10.1016/j.actamat.2011.08.016.

[72] A. Misra, J.P. Hirth, H. Kung, Single-dislocation-based strengthening mechanisms in nanoscale metallic multilayers, Philos. Mag. A. 82 (2002) 2935–2951. doi:10.1080/01418610208239626.

[73] D. Pan, A. Inoue, T. Sakurai, M.W. Chen, Experimental characterization of shear transformation zones for plastic flow of bulk metallic glasses, Proc. Natl. Acad. Sci. 105 (2008) 14769–14772. doi:10.1073/pnas.0806051105.

[74] A.C. Fischer-Cripps, Nanoindentation, 2nd ed., Springer-Verlag, New York, 2004. //www.springer.com/la/book/9780387220451 (accessed August 31, 2018).

[75] B.E. Schuster, Q. Wei, T.C. Hufnagel, K.T. Ramesh, Size-independent strength and deformation mode in compression of a Pd-based metallic glass, Acta Mater. 56 (2008) 5091–5100. doi:10.1016/j.actamat.2008.06.028.

[76] S.Y. Kuan, H.S. Chou, M.C. Liu, X.H. Du, J.C. Huang, Micromechanical response for the amorphous/amorphous nanolaminates, Intermetallics. 18 (2010) 2453–2457. doi:10.1016/j.intermet.2010.09.001.

[77] Y.Y. Lu, R. Kotoka, J.P. Ligda, B.B. Cao, S.N. Yarmolenko, B.E. Schuster, Q. Wei, The microstructure and mechanical behavior of Mg/Ti multilayers as a function of individual layer thickness, Acta Mater. 63 (2014) 216–231. doi:10.1016/j.actamat.2013.10.032.

[78] Z.Q. Hou, J.Y. Zhang, J. Li, Y.Q. Wang, K. Wu, G. Liu, G.J. Zhang, J. Sun, Phase transformation-induced strength softening in Ti/Ta nanostructured multilayers: Coherent interface vs phase boundary, Mater. Sci. Eng. A. 684 (2017) 78–83. doi:10.1016/j.msea.2016.12.040.

[79] R.G. Hoagland, R.J. Kurtz, C.H. Henager, Slip resistance of interfaces and the strength of metallic multilayer composites, Scr. Mater. 50 (2004) 775–779. doi:10.1016/j.scriptamat.2003.11.059.

[80] R.C. Cammarata, Surface and interface stress effects in thin films, Prog. Surf. Sci. 46 (1994) 1–38. doi:10.1016/0079-6816(94)90005-1.

[81] N. Bernstein, M.J. Aziz, E. Kaxiras, Amorphous-crystal interface in silicon: A tight-binding simulation, Phys. Rev. B. 58 (1998) 4579–4583. doi:10.1103/PhysRevB.58.4579.

[82] N. Mara, A. Sergueeva, A. Misra, A.K. Mukherjee, Structure and high-temperature mechanical behavior relationship in nano-scaled multilayered materials, Scr. Mater. 50 (2004) 803–806.

[83] Y. Zhu, Z. Li, M. Huang, Y. Liu, Strengthening mechanisms of the nanolayered polycrystalline metallic multilayers assisted by twins, Int. J. Plast. 72 (2015) 168–184. doi:10.1016/j.ijplas.2015.05.014.

[84] J. Gong, T. Benjamin Britton, M.A. Cuddihy, F.P.E. Dunne, A.J. Wilkinson, ⟨a⟩ Prismatic, ⟨a⟩ basal, and ⟨c+a⟩ slip strengths of commercially pure Zr by micro-cantilever tests, Acta Mater. 96 (2015) 249–257. doi:10.1016/j.actamat.2015.06.020.

[85] J. Gong, A.J. Wilkinson, A microcantilever investigation of size effect, solid-solution strengthening and second-phase strengthening for 〈a〉 prism slip in alpha-Ti, Acta Mater. 59 (2011) 5970–5981. doi:10.1016/j.actamat.2011.06.005.

[86] M.C. Liu, C.J. Lee, Y.H. Lai, J.C. Huang, Microscale deformation behavior of amorphous/nanocrystalline multilayered pillars, Thin Solid Films. 518 (2010) 7295–7299. doi:10.1016/j.tsf.2010.04.096.

[87] J. Musil, Hard and superhard nanocomposite coatings, Surf. Coat. Technol. 125 (2000) 322–330. doi:10.1016/S0257-8972(99)00586-1.

[88] C. Yuan, R. Fu, F. Zhang, X. Zhang, F. Liu, Microstructure evolution and mechanical properties of nanocrystalline zirconium processed by surface circulation rolling treatment, Mater. Sci. Eng. A. 565 (2013) 27–32. doi:10.1016/j.msea.2012.11.092.

[89] M.C. Liu, J.C. Huang, Y.T. Fong, S.P. Ju, X.H. Du, H.J. Pei, T.G. Nieh, Assessing the interfacial strength of an amorphous–crystalline interface, Acta Mater. 61 (2013) 3304–3313. doi:10.1016/j.actamat.2013.02.019.

[90] M.A. Meyers, A. Mishra, D.J. Benson, Mechanical properties of nanocrystalline materials, Prog. Mater. Sci. 51 (2006) 427–556. doi:10.1016/j.pmatsci.2005.08.003.

[91] C.-C. Yu, C.M. Lee, J.P. Chu, J.E. Greene, P.K. Liaw, Fracture-resistant thin-film metallic glass: Ultra-high plasticity at room temperature, APL Mater. 4 (2016) 116101. doi:10.1063/1.4966932.

APPENDICES

APPENDIX-A: THICKNESS CALIBRATION

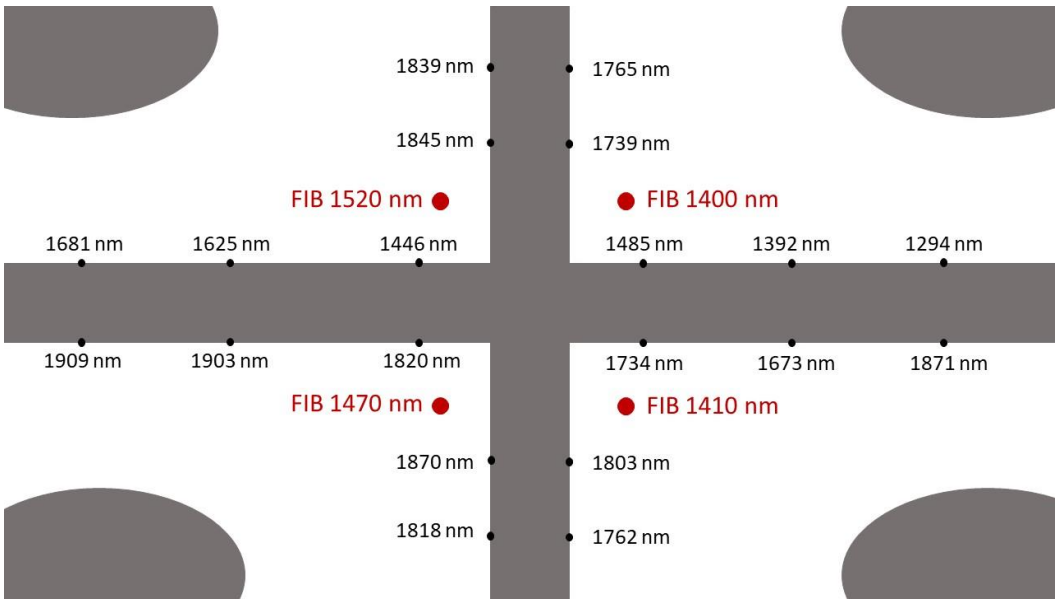

Figure A1. Profilometry measurement of a Zr film coated at 100 W for 120 min. Black markers indicate the positions of optical profilometry scans, while red markers indicate the positions of FIB cross-sections.

Figure A1 shows a large sample (2 cm x 3 cm) that was coated with a tape in the middle of it then later used to determine the thickness profile for 120 min of Zr DC coating at 100 W.

Up to 20% change in thickness can be observed in the sample, therefore, only a small portion of the sample was used in the thesis to reduce the error. Similar procedure was used to calibrate the sputtering rates of Cu and Ti. The sputtering rate was then assumed to decrease linearly as the power was decreased. At the selected area, FIB cross-sections were milled to double check the calibration. Figures A2 and A3 show the optical profilometry results one of the scans. 1 µm should be subtracted for the SiO2 layer since it is invisible to the laser.

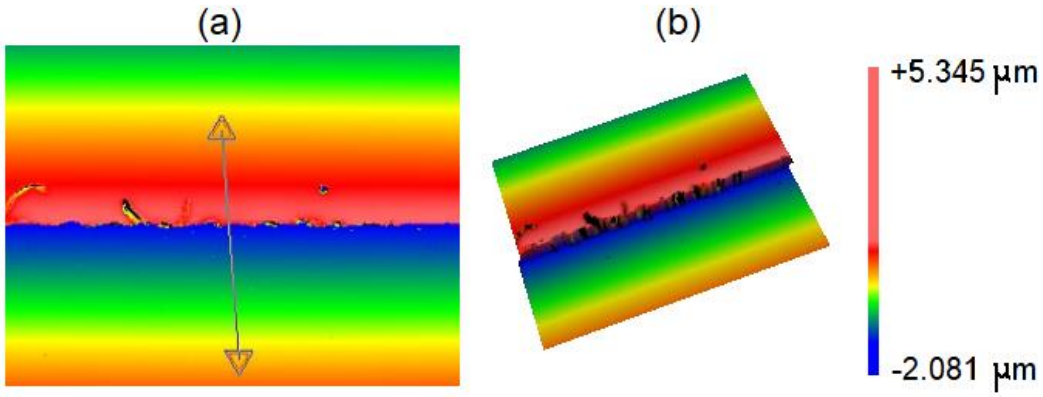

Figure A2. Profilometry measurements of a Zr film coated at 100 W for 120 min. Dimensions are in nm. (a) 2D model of the optical surface scan with a selected line scan. (b) 3D model of the optical surface scan.

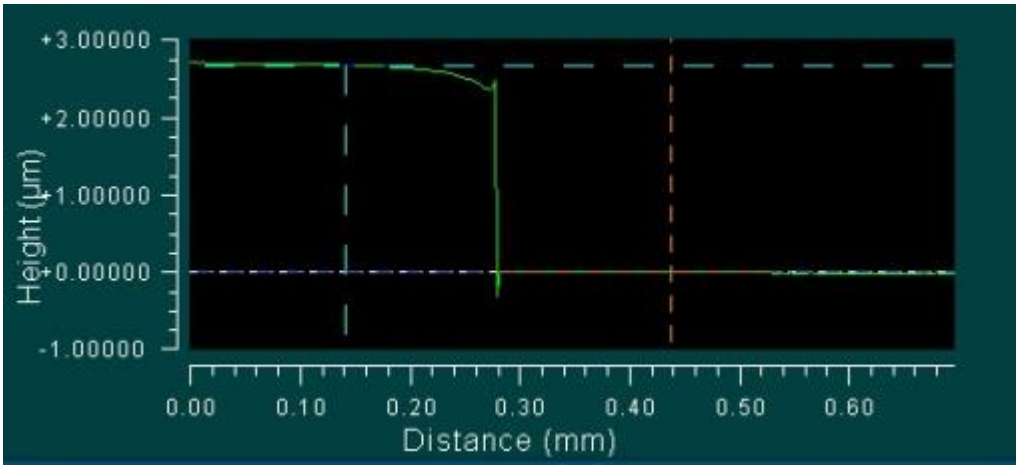

Figure A3. Surface profile obtained from figure A2. Levelling was done according to the SiO2 substrate.

APPENDIX-B: FIB PROCEDURE IMAGES

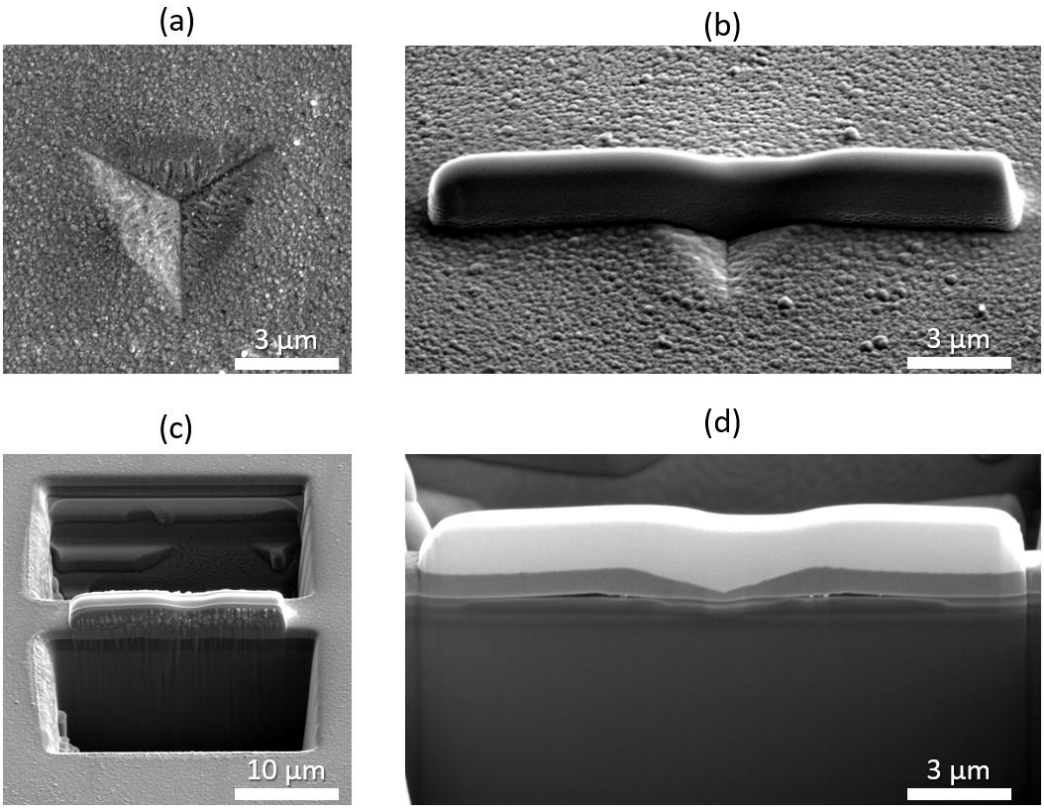

Figure B1. FIB cross-section of a nanoindentation on CuTi/Ti 50 nm. (a) The selected nanoindentation, (b) Platinum protective coating, (c) ion milled areas, and (d) the cross-section of the nanoindentation.

Figure B1 shows the steps taken to obtain a cross-section images. It is close to the center of a nanoindentation showing 800 nm depth. The sides of the image in figure B1-d show that the film is of a correct thickness. This sample was thinned, cut out, and used for TEM characterization. Similar procedure was followed to validate the thickness and microstructure of all the samples.

APPENDIX-C: CONFINED LAYER SLIP MODEL CALCULATIONS

According to the model, the normal stress required to propagate a glide loop of Burgers vector *b* within a single Cu layer can be estimated as:

$$\sigma_{cls} = \frac{M\mu b}{8\pi(h/sin(\varphi))} ln\left(\frac{\alpha}{b_{Cu}}\frac{h}{sin(\varphi)}\right)\left(\frac{4-\upsilon}{1-\upsilon}\right) - \frac{f}{h} + \frac{\mu b}{L(1-\upsilon)} \qquad (7)$$

Table C1. Values used for the CLS model calculations

Symbol	Meaning	Value for CuTi/Cu	Value for CuTi/Ti	Value for CuTi/Zr
M	Taylor factor	3.7	3.06	3.06
μ	effective shear modulus	20.3 GPa	20.3 GPa	20.3 GPa
b	length of the Burgers vector	0.26 nm	0.29 nm	0.32 nm
h	layer thickness	As mentioned in Chapter 2		
φ	angle between the glide plane and the interface	70.5°	60°	60°
v	Poisson's ratio	0.34	0.32	0.34
α	core cutoff parameter (< 1)	0.45	0.45	0.45
f	interface stress caused by the elastic deformation of the interface region	1.1 J/m^2	1.1 J/m^2	1.1 J/m^2
L	spacing between the parallel array of glide loops	5 nm	9 nm	9 nm
-	Tabor factor	2.7	2.7	2.7

By substituting the values in Equation (7), we can obtain σ_{cls} for every sample. Then using Equation (7) with a Tabor factor of 2.7, the hardness of each sample can be estimated as $H = 2.7\sigma_{cls}$.

APPENDIX-D: HRTEM

To further check the microstructure, HRTEM images were taken of selected areas within each sample. Figure D1a show the HRTEM image of CuZr/Zr-100. Figures D1b and c show fast Fourier transform at a selected section away from the interface. (b) shows the fast Fourier transform of a selected area from the amorphous section of the HRTEM image, while (c) shows fast Fourier transform of a selected area from the crystalline section of the HRTEM image.

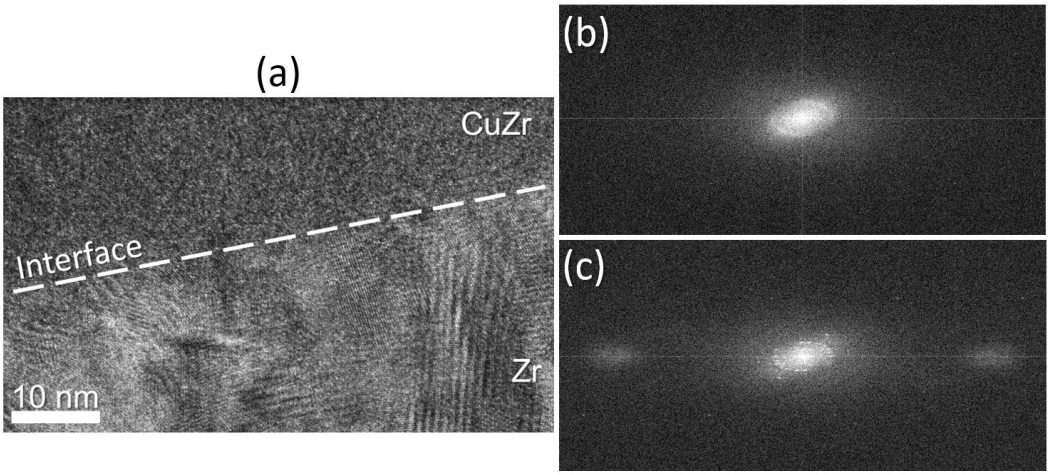

Figure D1. HRTEM of interface between the layers of CuZr/Zr-100. (a) HRTEM image, (b) fast Fourier transform of a selected area from the amorphous section of the HRTEM image and (c) fast Fourier transform of a selected area from the crystalline section of the HRTEM image.